

Experimental scattering matrices of levitated single millimeter-sized dust pebbles at visible wavelengths

Downloaded from: https://research.chalmers.se, 2026-11-15 21:59 UTC

Citation for the original published paper (version of record):
Garcia-Izquierdo, F., Passas-Varo, M., Frattin, E. et al (2026). Experimental scattering matrices of levitated single millimeter-sized dust pebbles at visible wavelengths. Astronomy and Astrophysics, 713. http://dx.doi.org/10.1051/0004-6361/202660347

N.B. When citing this work, cite the original published paper.

research.chalmers.se offers the possibility of retrieving research publications produced at Chalmers University of Technology. It covers all kind of research output: articles, dissertations, conference papers, reports etc. since 2004. research.chalmers.se is administrated and maintained by Chalmers Library

(article starts on next page)

A&A, 713, A198 (2026)
https://doi.org/10.1051/0004-6361/202660347
© The Authors 2026

Astronomy & Astrophysics

Experimental scattering matrices of levitated single millimeter-sized dust pebbles at visible wavelengths

Francisco J. García-Izquierdo[1,⋆], María Passas-Varo[1], Elisa Frattin[1], Olga Muñoz[1], Julia Martikainen[1,2,3], Angel Colin[4], Gonzalo Vargas[1], and Romain Bordes[5]

[1] Instituto de Astrofísica de Andalucía, Glorieta de la Astronomía, 18008 Granada, Spain
[2] Instituto de Astrofísica de Canarias, 38200 La Laguna, Tenerife, Spain
[3] Nordic Optical Telescope, Rambla José Ana Fernández Pérez 7, 38711 Breña Baja, Spain
[4] Universidad de Murcia, Edificio N° 9, Campus de Espinardo, 30100 Murcia, Spain
[5] Department of Chemistry and Chemical Engineering, Chalmers University of Technology, 41296 Gothenburg, Sweden

Received 10 April 2026 / Accepted 15 July 2026

ABSTRACT

Aims. This work investigates the photopolarimetric behavior of millimeter-sized levitated dust pebbles. A secondary goal is to bridge the gap in photopolarimetric knowledge between micron-sized dust clouds and centimeter-scale pebbles.
Methods. We studied a set of nine millimeter-sized volcanic ash pebbles from a natural palagonite bulk. The pebbles were characterized by their surface colors, sizes, and surface features. The pebbles were levitated using an acoustic levitator to isolate them during the experiments. Measurements of the scattering matrices were performed at scattering angles ranging from 3° to 177° at wavelengths of 488 nm and 640 nm at the Cosmic Dust Laboratory at the Instituto de Astrofísica de Andalucía.
Results. We compare our measured scattering matrices for the set of palagonite pebbles with those of micron-sized dust clouds of similar composition, revealing clear differences between the two size regimes. The main differences emerge from the phase function and the degree of linear polarization (DLP) curves. The pebbles exhibit a U-shaped phase function with minima of between 16° and 33°, whereas clouds of micron-sized dust particles show a nearly flat behavior at side- and back-scattering regions. The DLP curves of the pebbles exhibit maxima of between 48° and 66°, whereas micron-sized powders tend to have them close to or beyond 90°. The negative polarization branch (NPB) of the pebbles closely resembles that of micron-sized dust particles with effective radii lying at the transition between the resonance and geometric optics regimes at visible wavelengths. This indicates that the use of the NPB features as a proxy for the maximum of the DLP curves must be taken with caution. Additionally, we evaluate the range of applicability of the linear-exponential model to fit the NPB. The retrieved key polarimetric parameters are clearly affected by the pebbles' chemical composition. They also enable a preliminary comparison of the pebbles to the asteroid taxonomy due to the strong similarities between their DLP curves.

Key words. polarization – scattering – techniques: polarimetric – minor planets, asteroids: general

1. Introduction

Cosmic dust plays a fundamental role in many astronomical environments, as it scatters and absorbs the light emitted by stars. These light-matter interactions directly influence radiative processes in the regions where they occur. The outcome of these processes is strongly dependent on the physical properties of the dust, such as particle size, chemical composition, and morphology. Consequently, the analysis of scattered light becomes a powerful tool for inferring the properties of cosmic dust. In this context, the study of scattering behavior has been applied in different astrophysical frameworks (Kolokolova et al. 2015; Bagnulo et al. 2024), particularly through observations of comets (Kolokolova et al. 2024) and asteroids (Belskaya et al. 2015; Li et al. 2015). In astronomical observations, scattering properties are commonly characterized by measuring the phase function (the angular distribution of the scattered light) and the degree of linear polarization (DLP) (Delahodde et al. 2001; Boehnhardt et al. 2008; Ishiguro et al. 2017; Kuroda et al. 2021). Furthermore, multispectral measurements of these quantities allow for the use of additional diagnostic tools, such as the determination of spectral color and polarimetric color of astronomical bodies (Kolokolova et al. 2001; Kwon et al. 2019; Fornasier et al. 2020; Alvarez-Candal 2024).

The shapes of the phase function and the DLP show the effect of dust physical properties. In most astronomical observations of dust clouds, the phase function exhibits a pronounced forward-scattering peak and a weaker, flatter backscattering region. This characteristic shape is typically associated with micron-sized dust grains and has been confirmed in laboratory experiments (Munoz et al. 2001; Volten et al. 2007; Dabrowska et al. 2015; Frattin et al. 2019; Gómez-Martín et al. 2023; Martikainen et al. 2024). Interest in larger particles has increased following observations of comet 67P/Churyumov-Gerasimenko by the ESA Rosetta mission (Rotundi et al. 2015; Ott et al. 2017; Della Corte et al. 2019). Phase functions obtained with the OSIRIS instrument indicated that the scattered light from the comet's dusty coma was dominated by particles larger than initially anticipated (Bertini et al. 2017; Moreno et al. 2018; Levasseur-Regourd et al. 2019; Muñoz et al. 2020). Particle size also strongly affects the DLP, particularly the angular position of the maximum polarization. For millimeter-sized particles, it occurs at scattering angles smaller than 90°, whereas for micron-sized particles it is usually found beyond 90° (Frattin et al. 2022). In addition to size, other physical properties provide specific DLP features,

⋆ Corresponding author: fgarcia@iaa.es

Open Access article, published by EDP Sciences, under the terms of the Creative Commons Attribution License (https://creativecommons.org/licenses/by/4.0), which permits unrestricted use, distribution, and reproduction in any medium, provided the original work is properly cited.
This article is published in open access under the Subscribe to Open model. Subscribe to A&A to support open access publication.

such as the negative polarization branch (NPB) (Shkuratov et al. 2004; Muinonen et al. 2011; Grynko et al. 2022). The NPB is a well-known feature in asteroid polarimetry and has been widely used for taxonomic classification (Belskaya et al. 2017, 2022). Astronomical observations often provide limited angular coverage to fully reconstruct the NPB, so empirical and semiempirical models have been developed to retrieve its key parameters (Goidet-Devel et al. 1995; Kaasalainen et al. 2003; Muinonen et al. 2009b). Nevertheless, accurately modeling irregular cosmic dust remains challenging due to the complex morphologies and wide size distribution of the particles. For spherical grains, Lorenz-Mie theory can be applied to compute the scattering pattern without any restriction of size or composition (Mie 1908; van de Hulst 1981). For irregular particles, more sophisticated numerical techniques have been developed (Mishchenko 2015; Muinonen et al. 2015; Kahnert et al. 2016; Kimura et al. 2016; Kolokolova et al. 2024; Vargas et al. 2026). While these methods are efficient for particles with sizes comparable to the incident wavelength, they become computationally expensive and time-consuming for significantly larger particles. As a result, the scattering behavior of millimeter-sized particles at visible wavelengths remains poorly understood. In this context, laboratory experiments using millimeter-sized particles become an essential tool for exploring this size regime and for validating advanced numerical models in the geometric optics domain developed by, for example, Muinonen et al. (2009a), Nousiainen (2009), and Grynko et al. (2016).

The Cosmic Dust Laboratory at the Instituto de Astrofísica de Andalucía (IAA-CoDuLab; (Muñoz et al. 2010, 2011)) obtains experimental scattering matrices of cosmic dust and analog materials, while the Granada-Amsterdam Light Scattering Database (Muñoz et al. 2025) contains all datasets obtained. CoDuLab has recently been upgraded to enable the measurement of scattering matrices from individual millimeter-sized particles. This advancement is based on the incorporation of an acoustic levitator, which allows particles to be suspended in air (Marzo et al. 2017; Colin et al. 2025), thereby avoiding the need for mechanical holders (Muñoz et al. 2017, 2020).

In this work, Section 2 describes the experimental setup, detailing the recent adaptation of the instrument and the calibration tests for the measurements presented here. Section 3 introduces the samples used in this study and the characterization of their physical properties. Section 4 reports the experimental scattering matrices at 488 nm and 640 nm. In Section 5, we compare our results with those obtained for dust of similar composition in order to constrain the effect of particle size on the scattering matrix elements. In addition, we analyze our measurements as if they corresponded to asteroid observations, seeking similarities and differences through the study of the NPB. Finally, Section 6 summarizes the main findings of the work and presents the conclusions.

2. Experimental setup

The experimental measurements were performed at the Cosmic Dust Laboratory (CoDuLab; Muñoz et al. (2010)) of the Instituto de Astrofísica de Andalucía (IAA). The different light scattering apparatus configurations allow for the study of micron-sized particle clouds using an aerosol generator (Frattin et al. 2019; Muñoz et al. 2021; Gómez-Martín et al. 2021), as well as individual millimeter-sized pebbles (Muñoz et al. 2020; Frattin et al. 2022) or analog regolith surfaces (Frattin et al. 2025; García-Izquierdo et al. 2026) mounted on a dedicated holder. For smaller millimeter-scale pebbles, the setup was further adapted to incorporate an acoustic levitator (Colin et al. 2025). The levitator was based on the design introduced by Marzo et al. (2017) and that relies on two arrays of 36 ultrasonic transducers operated at 40 kHz (Figure 1). The arrays are semi-spherical and create a stable standing wave in air. The node of this stationary wave, where pebbles are trapped, is located at the center of the instrument.

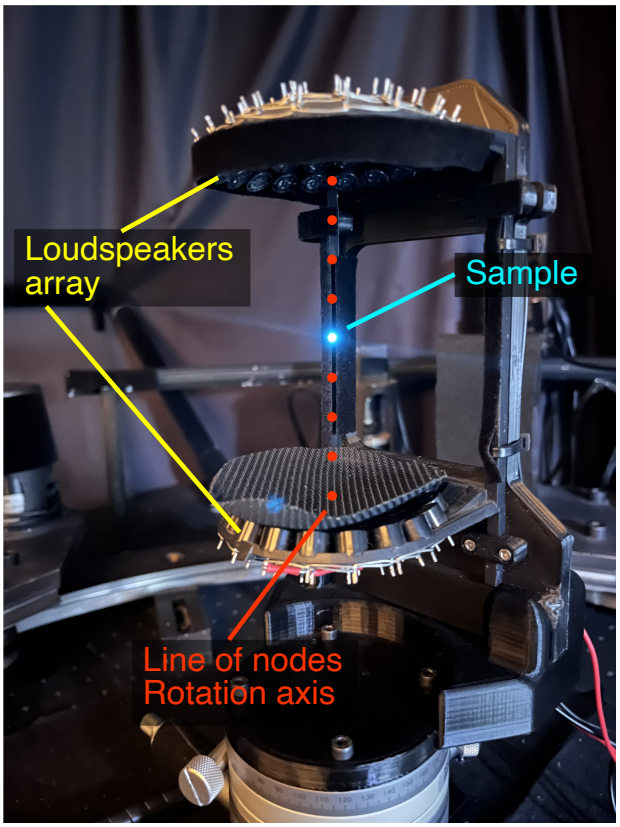


Fig. 1. Picture of the ultrasonic acoustic levitator mounted on the optical bench at CoDuLab.

Figure 2 presents a schematic view of the adapted experimental setup. The light source is a Coherent High Performance OBIS^{TM} laser operating at either 488 nm or 640 nm. A motorized filter wheel (FW) equipped with neutral-density filters is positioned between the laser and the polarizer (P) to control the beam intensity. The polarizer is coupled to an electro-optic modulator (M), which modulates the polarization state of the incident light. After modulation, the beam is expanded using a beam expander to ensure homogeneous-full illumination of the pebbles. The final beam diameter is adjusted with a diaphragm (D).

During levitation, the pebbles spin rapidly along the vertical axis (see Figure 1). This is the line of nodes of the stationary ultrasonic wave, which is perpendicular to the laser propagation direction. This continuous rotation allows the scattered signal to include contributions from multiple particle orientations. During the rotation, the pebbles tend to include their two largest axes in the scattering plane. The scattered light is detected by a photomultiplier tube (PM detector), operating at a sampling rate of 1000 measurements per 1.5 s. The detector moves along one meter diameter circular rail, covering scattering angles from 3° to 177°. The scattering angle, θ, is defined as the angle between the incident beam and the observation direction. A second photomultiplier tube (PM monitor), fixed at 71°, provides a reference

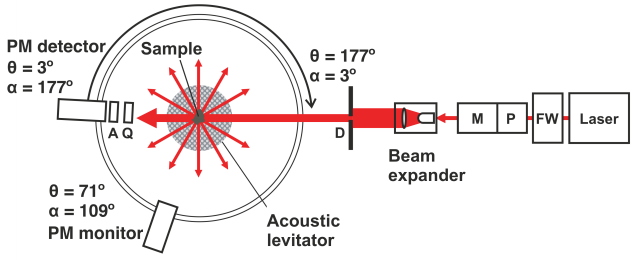


Fig. 2. Top-view schematic of the adapted CoDuLab optical train as seen from above. FW = filter wheel, P = polarizer, M = modulator, D = diaphragm, A = analyzer, Q = quarter wave plate, and PM = photomultiplier.

signal to correct for intensity variations due to the FW and source fluctuations. The PM monitor has the same sampling rate as the PM detector. Before reaching the PM detector, the scattered light may pass through optional optical elements, such as an analyzer (A) and a quarter wave plate (Q), depending on the optical configuration required to obtain specific combinations of scattering matrix elements, F_{ij}. Together with electro-optical modulation of the incident beam and lock-in detection, this setup enables the determination of F_{ij} or combinations of them per measurement run (see Muñoz et al. (2010) for details). By using the optional optic elements at different orientations, the various F_{ij} can be determined experimentally.

These elements form the 4×4 scattering matrix, which relates the Stokes vector of the incident light, (I_0, Q_0, U_0, V_0), to that of the scattered light, (I_S, Q_S, U_S, V_S). The F_{ij} are dimensionless quantities which depend on the wavelength of the incident radiation and on the physical properties of the scatterers. In addition, symmetry properties of the samples may force certain elements to vanish and impose relationships among others, resulting in a simplified form of the scattering matrix (van de Hulst 1981; Hovenier et al. 2014).

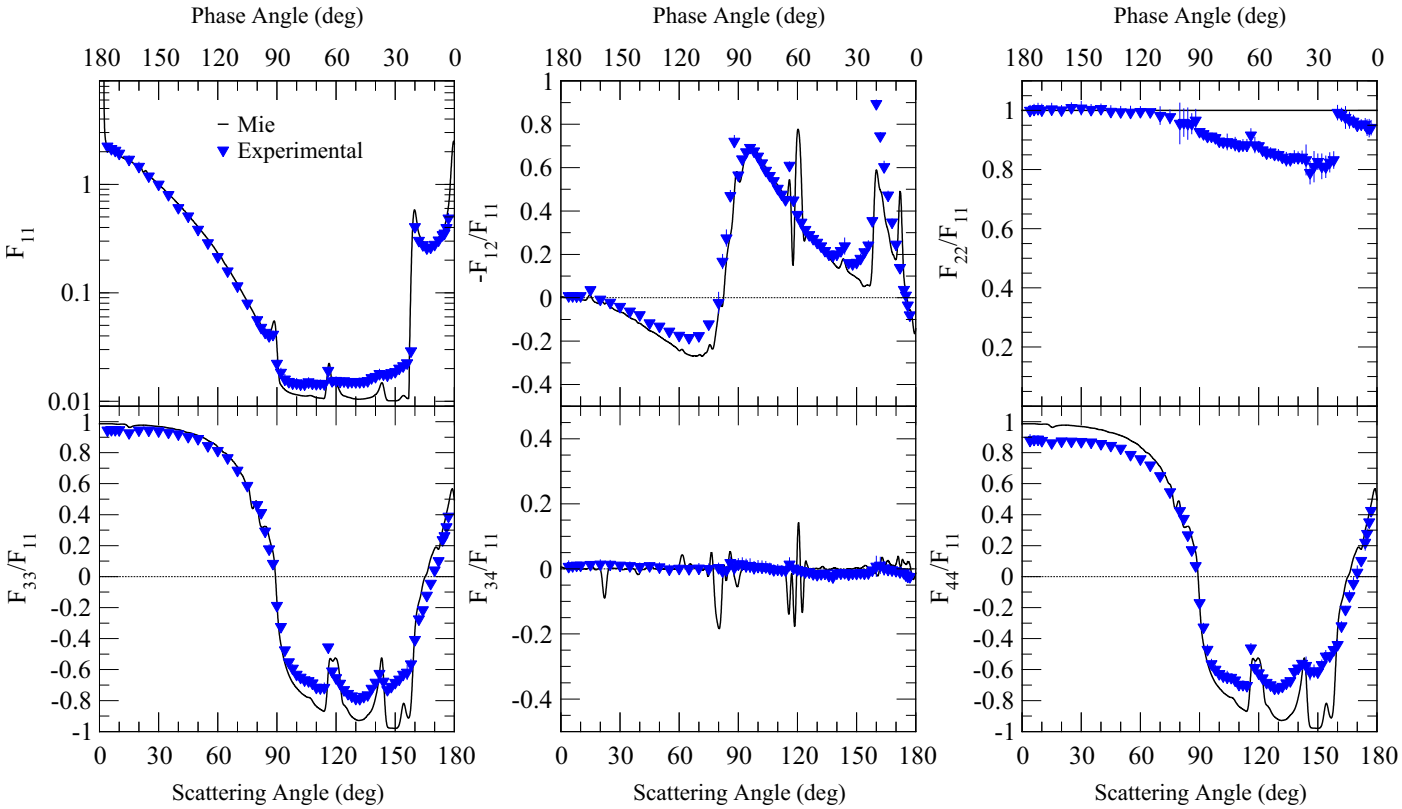
For unpolarized incident light, the element $F_{11}(\theta)$ is proportional to the scattered intensity and is commonly referred to as the phase function. In this case, the ratio $-F_{12}(\theta)/F_{11}(\theta)$ defines the DLP. In planetary science, the F_{ij} are typically expressed as a function of the phase angle, defined as $\alpha = 180^\circ - \theta$.

To validate the experimental configuration incorporating the acoustic levitator, we measured the $F_{ij}(\theta)$ of a NBK-7 calibration sphere made of borosilicate crown glass, with a radius of 750 µm and a sphericity of 0.625 µm, supplied by Edmund Optics. The sphere radius was selected to match the characteristic size of the pebbles under investigation. The refractive indices of the NBK-7 sphere at 488 nm and 640 nm are $m(488\text{ nm}) = 1.5222 + i\,9.7905 \cdot 10^{-9}$ and $m(640\text{ nm}) = 1.5148 + i\,1.226 \cdot 10^{-8}$, respectively (Polyanskiy 2024). Figure 3 shows the experimental results together with the theoretical F_{ij} computed using Mie theory (Mie 1908). The measurements reproduce the main features predicted by Mie theory with good accuracy. However, some deviations from the theoretical curves are observed. These discrepancies arise because light scattered by the sphere in all directions is reflected by the acoustic levitator structure and subsequently reaches the detector. Such effects are stronger in the scattering angle range from 90° to 150°, where $F_{11}(\theta)$ reaches its minimum. In this low-signal region (where the intensity is orders of magnitude lower than at other angles) stray reflections from the levitator become noticeable, introducing a partially depolarized contribution. These effects are significant in $F_{22}(\theta)/F_{11}(\theta)$, $F_{33}(\theta)/F_{11}(\theta)$, and $F_{44}(\theta)/F_{11}(\theta)$. Moreover, the field of view of the PM detector integrates the scattered signal over a small angular range, smoothing fine structures in some F_{ij}, such as $F_{34}(\theta)/F_{11}(\theta)$. Nevertheless, the pebbles under study are significantly less reflective than the NBK-7 calibration sphere, and their phase functions are not expected to span several orders of magnitude. Therefore, the contribution of stray reflections from the levitator would be significantly smaller than in the measurements of the pebbles.

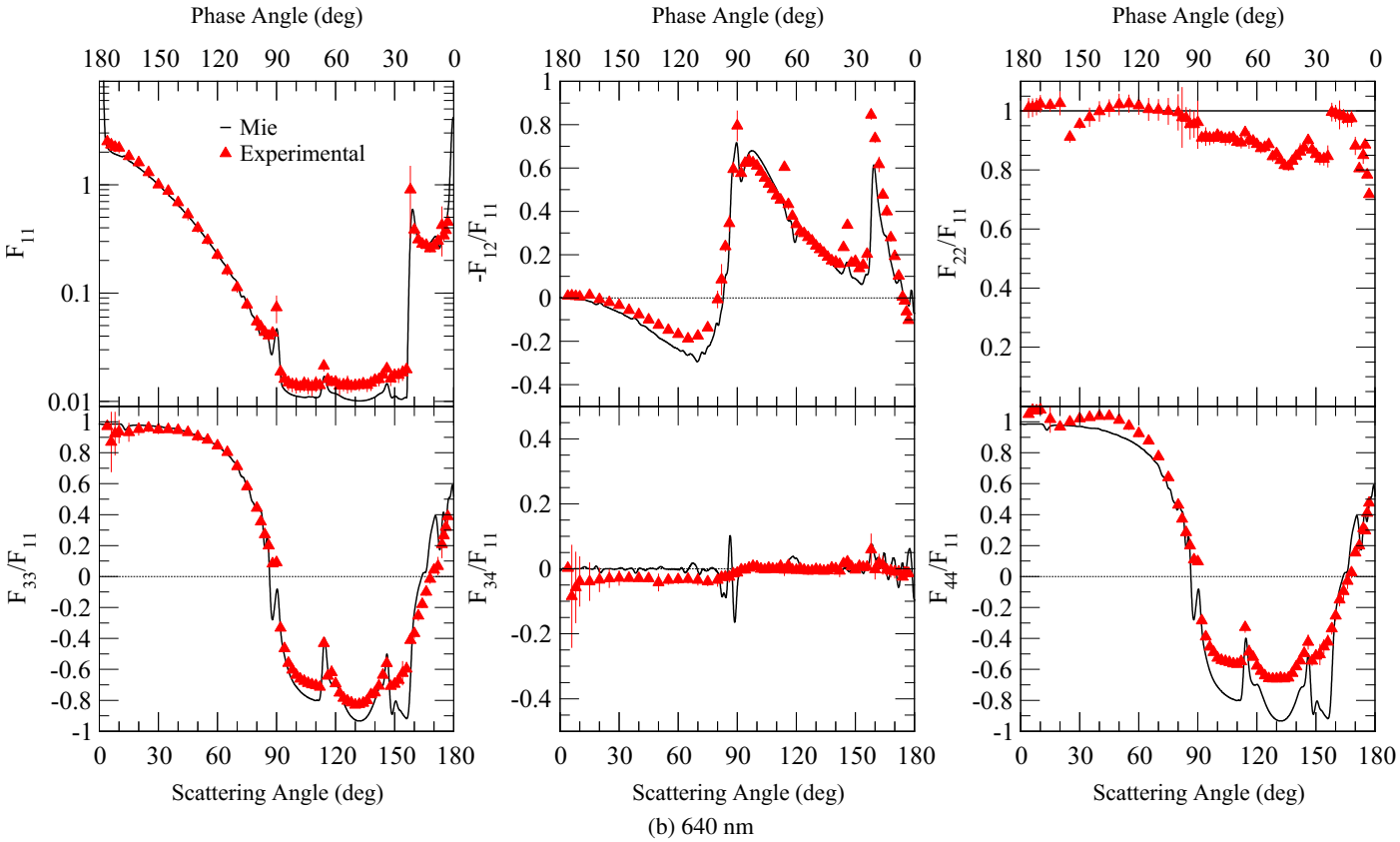
3. Sample description

In this work, we investigated nine millimeter-sized pebbles composed of palagonite (Laan et al. 2009), a weathering product of basaltic glass. This bulk material contains a significant fraction of Fe_2O_3 (Roush & Bell III 1995) and corresponds to the sample 91-16 collected at the Mauna Kea volcano, in Hawaii. A detailed characterization of this material can be found in Banin et al. (1997). The millimeter-sized pebbles were individually selected to cover a range of color tones and sizes. As the bulk material can be used as Martian analog, we named each pebble MAVAP (Martian Analog Volcanic Ash Pebble), followed by an index from 1 to 9. Figure 4 shows optical microscopy images of the MAVAPs obtained under identical illumination conditions. These images provide information about their apparent color to the naked eye, allowing for a classification into "dark" and "light" MAVAPs. Dark MAVAPs correspond to the indices 1, 4, 6, 7, and 9, whereas light MAVAPs correspond to the indices 2, 3, 5, and 8. The optical images do not provide reliable size information, as the three-dimensional morphology of the MAVAPs produces blurring effects due to different focal planes.

We estimated the size of the MAVAPs by measuring their projected area while levitated. Their orientation on a flat surface may differ from that during levitation, which determines the effective area exposed to the laser and thus relevant for scattering. For this purpose, the shadow of each MAVAP was projected onto a millimeter-graduated screen and photographed. This procedure provides a conversion from pixels to physical area units (square millimeters). By determining the number of pixels covering each projected shadow, the corresponding projected area can be calculated. The measurement was repeated seven times for each MAVAP in order to obtain an average value. Figure 5 shows the superposition of the seven projected areas for each MAVAP. This representation provides an estimate of the effective size as seen by the laser beam and illustrates the blurred boundaries produced by the rotational motion during levitation. To validate the reliability of this method, we performed the same procedure using a calibrated sphere with a nominal diameter of 3 mm. The measured projected area corresponds to a circle with a diameter of 3.031 ± 0.005 mm. In addition, the projected contour was fit with an ellipse to determine the eccentricity (the ratio between the major and minor axes). For the calibrated sphere, the eccentricity is 1.005 ± 0.003, consistent with an almost perfectly circular projected shape. Table 1 summarizes the measured projected areas for MAVAPs, the diameters of the best-fitting ellipses and their corresponding eccentricities. During the experiments, the major axis of the projected ellipse lies within the scattering plane. The measured areas range from 0.31 ± 0.02 mm^2 (MAVAP-6) to 2.5 ± 0.2 mm^2 (MAVAP-1), covering particle sizes from submillimeters to a few millimeters. Most MAVAPs exhibit similar eccentricities, with values between 1.4 and 1.59. The lowest eccentricity is found for MAVAP-4, with a value of 1.28 ± 0.03, whereas the highest values correspond to MAVAP-7 and MAVAP-8, with eccentricities of 2.0 ± 0.2 and 2.1 ± 0.1, respectively. Within our sample set, no correlation is observed between size, shape, and color.



(a) 488 nm



(b) 640 nm

Fig. 3. Comparison between experimental data and Mie theory for a 750 µm radius NBK-7 sphere at 488 nm and 640 nm.

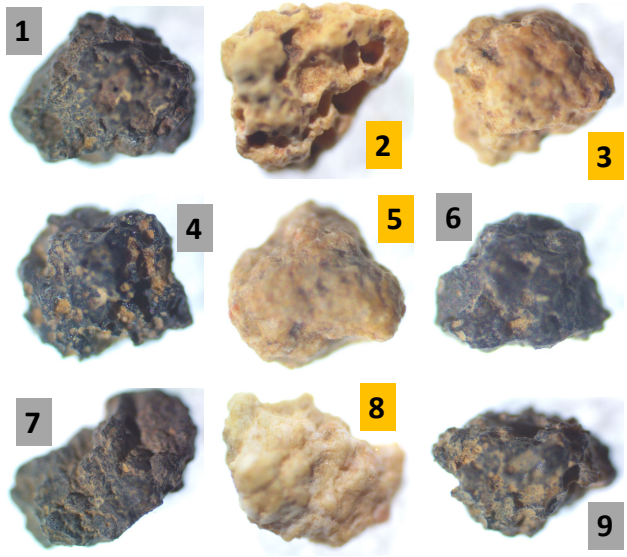


Fig. 4. Images under optical microscope with same illumination conditions for MAVAPs. Numbers indicate the index of each sample.

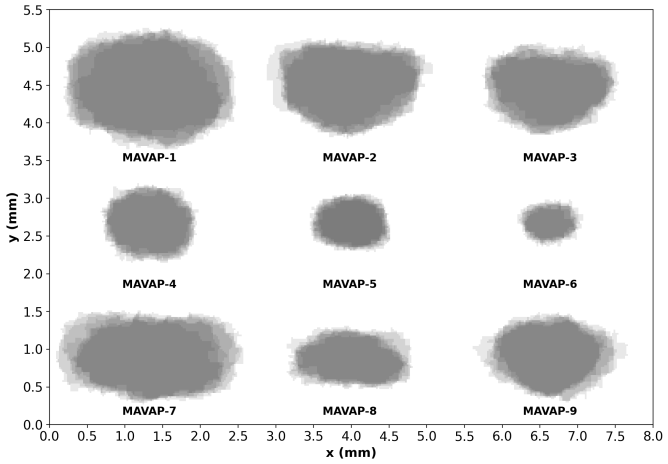


Fig. 5. Projected areas for MAVAPs. For each MAVAP there are seven shades matching the position of their centroids.

Table 1. Size characterization of MAVAPs through their projected shades.

MAVAP	Area (mm^2)	D$_{max}$eq (mm)	D$_{min}$eq (mm)	Eccentricity
1	2.5 ± 0.2	2.1 ± 0.1	1.44 ± 0.03	1.4 ± 0.1
2	1.76 ± 0.05	1.8 ± 0.1	1.17 ± 0.02	1.59 ± 0.09
3	1.37 ± 0.05	1.61 ± 0.09	1.08 ± 0.05	1.5 ± 0.1
4	0.89 ± 0.02	1.16 ± 0.03	0.91 ± 0.02	1.28 ± 0.03
5	0.57 ± 0.03	0.98 ± 0.04	0.68 ± 0.02	1.46 ± 0.07
6	0.31 ± 0.02	0.72 ± 0.05	0.52 ± 0.02	1.4 ± 0.1
7	2.0 ± 0.2	2.2 ± 0.2	1.10 ± 0.03	2.0 ± 0.2
8	0.89 ± 0.07	1.5 ± 0.1	0.71 ± 0.02	2.1 ± 0.1
9	1.3 ± 0.2	1.5 ± 0.2	1.04 ± 0.05	1.5 ± 0.1

To characterize the surface morphology of the MAVAPs, scanning electron microscopy (SEM) images were acquired. Figure 6 shows SEM images of the complete pebbles together with selected high-magnification regions. These images reveal the external morphology of the MAVAPs at micrometer scale. All MAVAPs exhibit features consistent with the typical morphology of vesicular volcanic grains. The magnified images further reveal that all MAVAPs are coated by a dusty envelope composed of nanometric particles of the same bulk material. No significant differences in sub-micrometric surface roughness are observed among the MAVAPs.

Table 2. Scattering angle at phase function minimum for MAVAPs at 488 nm and 640 nm.

	θ_{min} (deg)	
MAVAP	488 nm	640 nm
1	25 ± 1	22 ± 1
2	21 ± 1	18 ± 1
3	22 ± 1	18 ± 1
4	27 ± 1	24 ± 1
5	22 ± 1	16 ± 1
6	33 ± 3	29 ± 1
7	20 ± 1	23 ± 1
8	20 ± 1	17 ± 1
9	28 ± 1	22 ± 1

4. Results

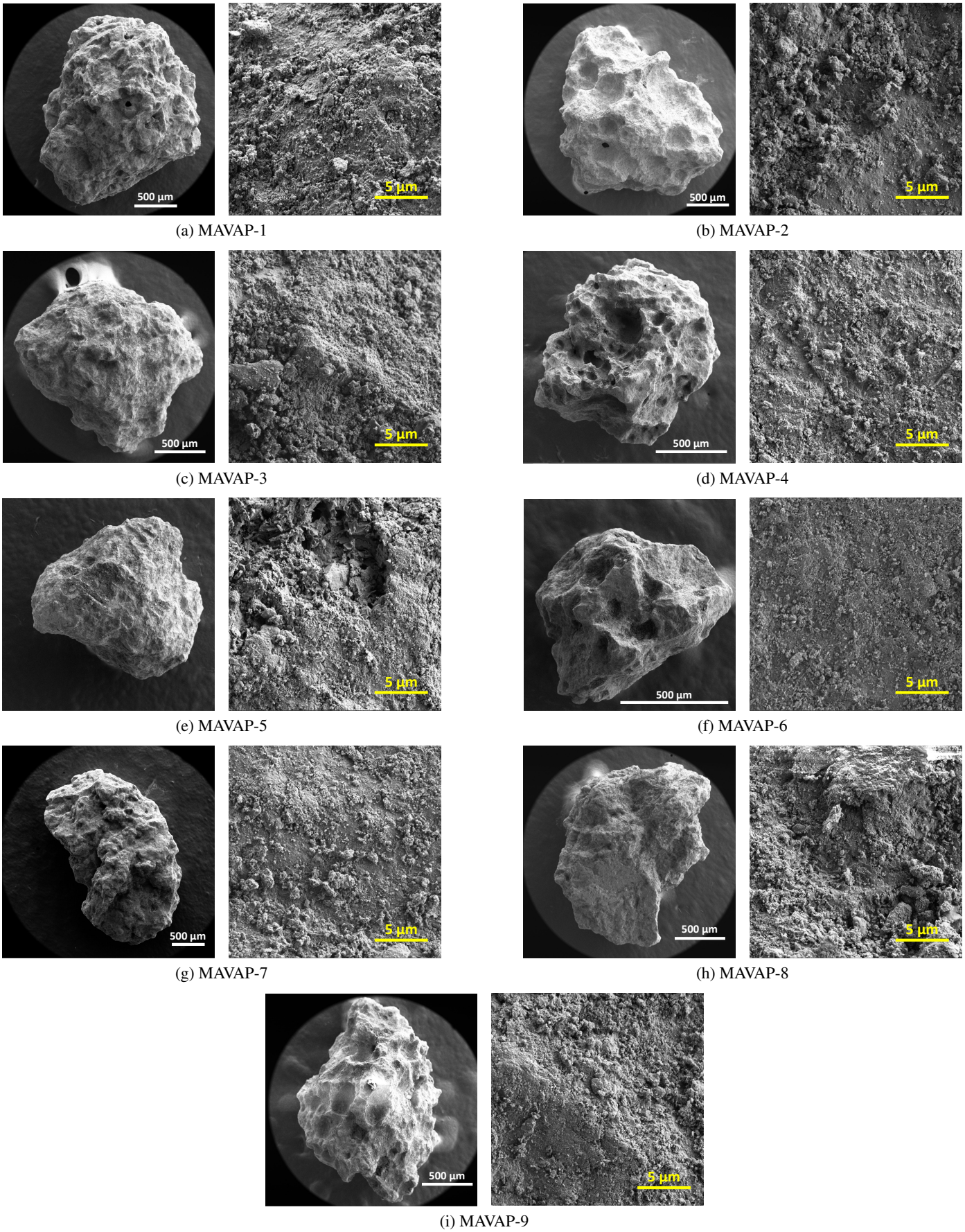
The experimental scattering matrices of the MAVAPs are shown in Figures 7, 8, and 9 at both 488 nm (blue circles) and 640 nm (red squares). The F_{ij} are displayed vertically as functions of scattering angle (and equivalently phase angle), in the following order: $F_{11}(\theta)$, $-F_{12}(\theta)/F_{11}(\theta)$, $F_{22}(\theta)/F_{11}(\theta)$, $F_{33}(\theta)/F_{11}(\theta)$, $F_{34}(\theta)/F_{11}(\theta)$, and $F_{44}(\theta)/F_{11}(\theta)$. Figure 7 presents the results for MAVAP-1, MAVAP-2, and MAVAP-3, Figure 8 shows those for MAVAP-4, MAVAP-5, and MAVAP-6, and Figure 9 displays the measurements for MAVAP-7, MAVAP-8, and MAVAP-9. The measurements cover a scattering angle range from 3° to 177°. In some cases, the forward-scattering region is truncated for certain F_{ij} due to a reduced signal-to-noise ratio at small scattering angles. We do not present element ratios $F_{13}(\theta)/F_{11}(\theta)$, $F_{14}(\theta)/F_{11}(\theta)$, $F_{24}(\theta)/F_{11}(\theta)$, $F_{31}(\theta)/F_{11}(\theta)$, and $F_{41}(\theta)/F_{11}(\theta)$, as they were found to be zero, and the equalities $F_{21}(\theta)/F_{11}(\theta) = -F_{12}(\theta)/F_{11}(\theta)$ and $F_{43}(\theta)/F_{11}(\theta) = -F_{34}(\theta)/F_{11}(\theta)$ are satisfied, across the full measured scattering angle range within the experimental error bars. Figure A.1 in Appendix A presents the measured matrix element ratios of one MAVAP as an example.

4.1. Phase function

The upper panels of Figures 7, 8, and 9 display the phase function, $F_{11}(\theta)$, for each MAVAP. All phase functions are normalized to unity at a scattering angle of 30°. Regardless of size, shape, or color, all MAVAPs exhibit a well-defined U-shaped phase function. This behavior is characteristic of millimeter-sized particles under visible illumination (Muñoz et al. 2017, 2020). Table 2 summarizes the angular position of the $F_{11}(\theta)$ minimum at both wavelengths. A slight trend with color is observed. At 640 nm, the light MAVAPs (2, 3, 5, and 8) show minima at scattering angles below 20°, whereas the dark MAVAPs (1, 4, 6, 7, and 9) present minima at angles larger than 20°. In addition, at 488 nm most minima are shifted toward larger scattering angles compared to their positions at 640 nm. MAVAP-7 appears to deviate from this general behavior. This case can be considered an outlier, since no other systematic trend is associated with it. Under these considerations, the position of the $F_{11}(\theta)$ minimum seems to be influenced primarily by the chemical composition of the MAVAPs.

4.2. Degree of linear polarization

The second panels from the top on Figures 7, 8, and 9 present the DLP, $-F_{12}(\theta)/F_{11}(\theta)$, for each MAVAP. Table 3



(a) MAVAP-1 (b) MAVAP-2

(c) MAVAP-3 (d) MAVAP-4

(e) MAVAP-5 (f) MAVAP-6

(g) MAVAP-7 (h) MAVAP-8

(i) MAVAP-9

Fig. 6. SEM images of MAVAPs. Each pair shows low-magnification (left) and high-magnification (right) views. Scale bars: white = 500 µm; yellow = 5 µm.

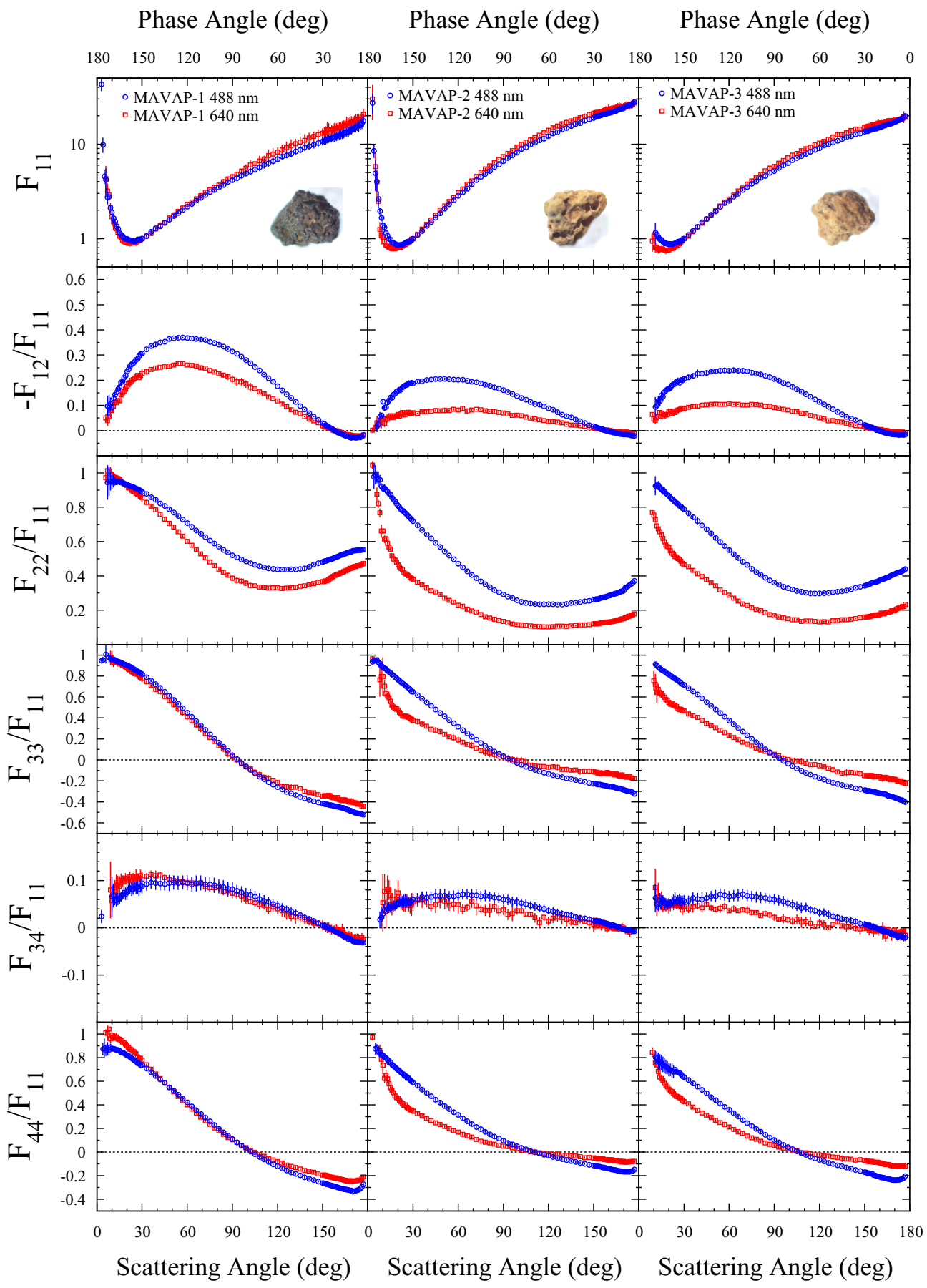


Fig. 7. Experimental scattering matrix elements as functions of the scattering angle at 488 nm (blue circles) and at 640 nm (red squares) for MAVAP-1 (left column), MAVAP-2 (middle column), and MAVAP-3 (right column).

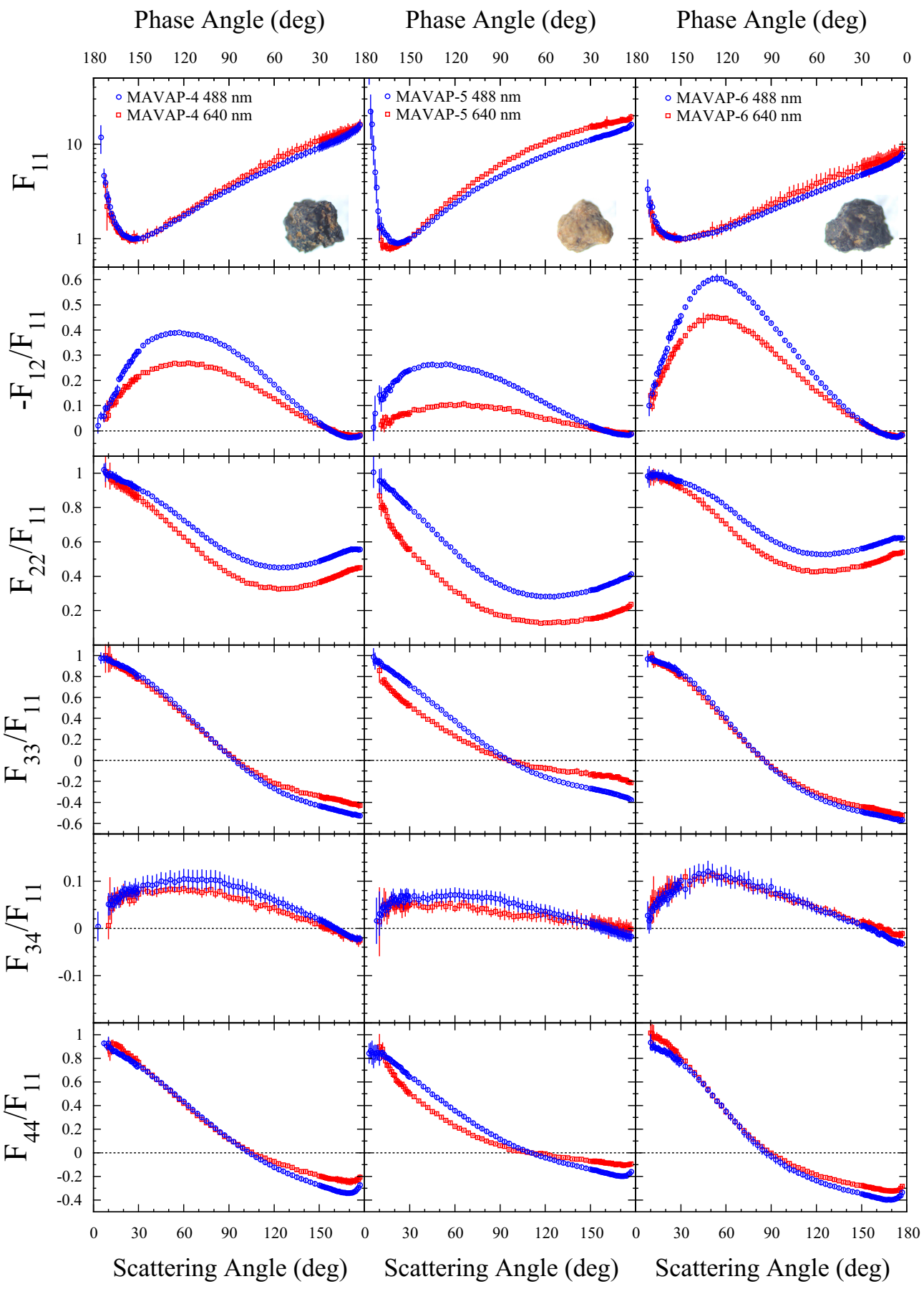


Fig. 8. Experimental scattering matrix elements as functions of the scattering angle at 488 nm (blue circles) and at 640 nm (red squares) for MAVAP-4 (left column), MAVAP-5 (middle column), and MAVAP-6 (right column).

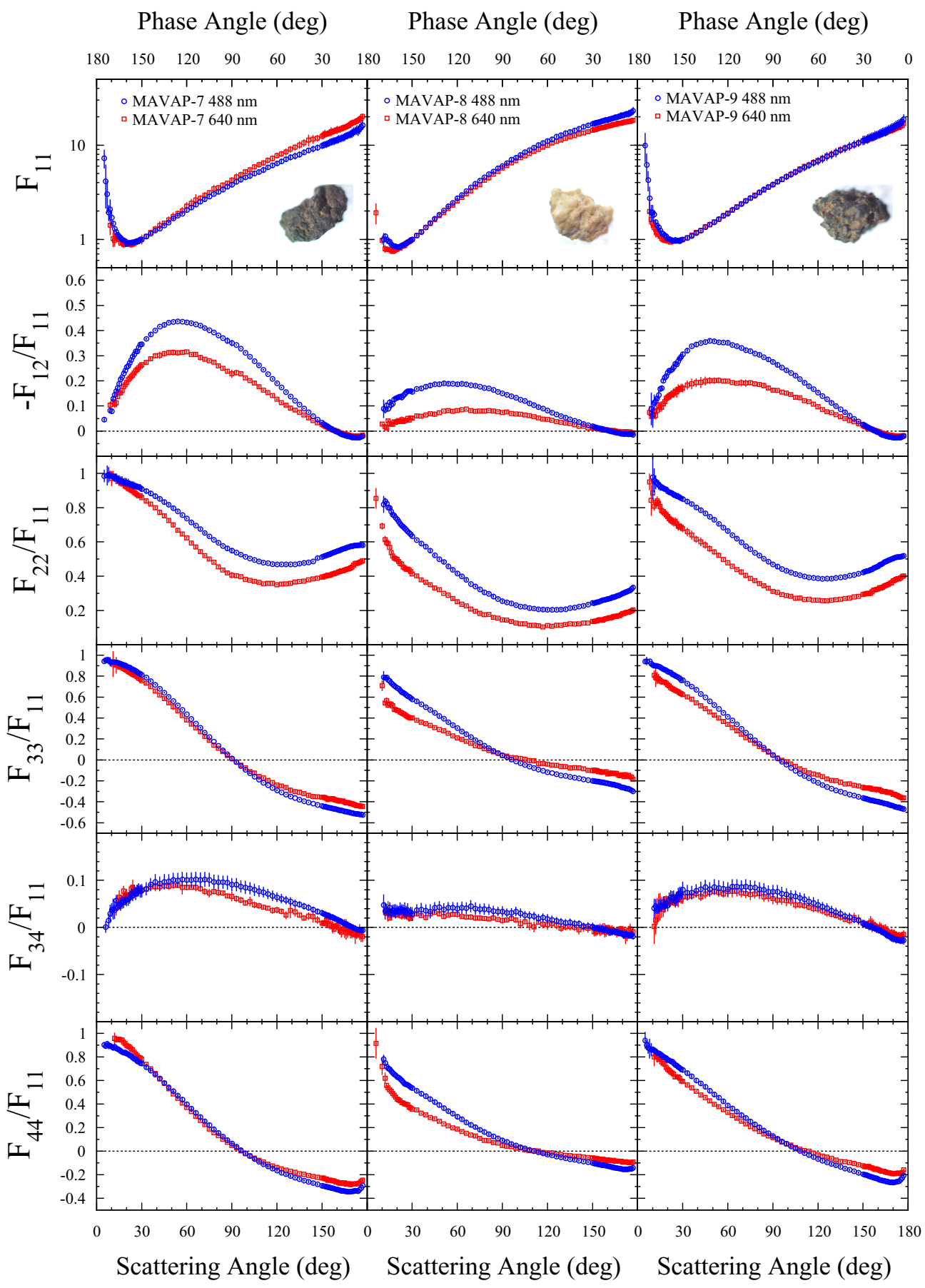


Fig. 9. Experimental scattering matrix elements as functions of the scattering angle at 488 nm (blue circles) and at 640 nm (red squares) for MAVAP-7 (left column), MAVAP-8 (middle column), and MAVAP-9 (right column).

Table 3. Experimental polarimetric parameters of the MAVAPs at 488 nm and 640 nm.

λ = 488 nm					
MAVAP	DLP_{min} (%)	θ_{min} (deg)	θ_{inv} (deg)	DLP_{max} (%)	θ_{max} (deg)
1	−2.8 ± 0.1	172 ± 1	158 ± 1	37.0 ± 0.1	57 ± 3
2	−2.0 ± 0.2	177 ± 1	158 ± 1	20.6 ± 0.3	51 ± 3
3	−1.8 ± 0.1	176 ± 1	160 ± 1	24.0 ± 0.8	63 ± 3
4	−2.6 ± 0.3	171 ± 1	158 ± 1	39.1 ± 0.1	57 ± 3
5	−1.8 ± 0.5	175 ± 1	160 ± 1	26.5 ± 0.1	54 ± 3
6	−2.5 ± 0.2	173 ± 1	160 ± 1	61 ± 1	54 ± 3
7	−2.5 ± 0.2	172 ± 1	159 ± 1	43.7 ± 0.2	54 ± 3
8	−1.4 ± 0.4	177 ± 1	162 ± 1	19.1 ± 0.5	51 ± 3
9	−2.6 ± 0.3	171 ± 1	158 ± 1	36.0 ± 0.4	48 ± 3
λ = 640 nm					
MAVAP	DLP_{min} (%)	θ_{min} (deg)	θ_{inv} (deg)	DLP_{max} (%)	θ_{max} (deg)
1	−2.2 ± 0.1	174 ± 1	158 ± 1	26.6 ± 0.5	54 ± 3
2	−1.2 ± 0.2	177 ± 1	160 ± 1	8.8 ± 0.7	63 ± 3
3	−0.9 ± 0.5	176 ± 1	162 ± 1	10.7 ± 0.3	60 ± 3
4	−2.1 ± 0.4	173 ± 1	160 ± 1	26.9 ± 0.5	63 ± 3
5	−1.0 ± 0.2	173 ± 1	163 ± 1	11 ± 1	66 ± 3
6	−2.3 ± 0.5	172 ± 1	160 ± 1	45 ± 1	51 ± 3
7	−2.0 ± 0.2	171 ± 1	160 ± 1	31.5 ± 0.4	60 ± 3
8	−0.7 ± 0.2	176 ± 1	167 ± 1	8.8 ± 0.1	66 ± 3
9	−2.1 ± 0.1	175 ± 1	160 ± 1	20 ± 1	54 ± 3

summarizes the main polarimetric parameters at both wavelengths. Specifically, the table lists the maximum DLP and its angular position (DLP_{max} and θ_{max}), the minimum and its angular position (DLP_{min} and θ_{min}), and the inversion angle (θ_{inv}), which is the angle at which the DLP changes sign, separating the positive polarization branch (PPB) from the NPB. All MAVAPs exhibit well-defined bell shape DLP curves.

Focusing on the PPB, the DLP_{max} is higher at 488 nm than at 640 nm for all MAVAPs. At 488 nm, light MAVAPs exhibit DLP_{max} between 19.1% and 26.5%, whereas dark MAVAPs exhibit it between 36% and 61%. At 640 nm, light MAVAPs exhibit DLP_{max} between 8.8% and 11%, while dark MAVAPs exhibit it between 20% and 45%. Since DLP_{max} increases with absorption (Dabrowska et al. 2015; Martikainen et al. 2024), these results indicate that dark MAVAPs are more absorbing than light MAVAPs, and that all MAVAPs exhibit stronger absorption at 488 nm than at 640 nm. The θ_{max} lies between 48° and 63° at 488 nm and between 54° and 66° at 640 nm. Although there is an apparent shift of θ_{max} toward smaller scattering angles at shorter wavelengths, no clear trends are observed. The θ_{max} is known to depend on particle size (Frattin et al. 2022), although the relative small size differences among the MAVAPs do not produce a clear trend within the geometric optics regime. Isolating size effects would be needed to assess possible shifts in θ_{max} in this size regime, since multiple physical properties may simultaneously affect its position.

Focusing on the backscattering region, all MAVAPs present a well-defined NPB at both wavelengths. The DLP_{min} is deeper at 488 nm than at 640 nm for all MAVAPs. At 488 nm, light MAVAPs exhibit DLP_{min} between −1.4% and −2%, whereas dark MAVAPs exhibit it between −2.5% and −2.8%. At 640 nm, light MAVAPs exhibit DLP_{min} between −0.7% and −1.2%, while dark MAVAPs exhibit it between −2% and −2.3%. These results indicate that stronger absorption is associated with a deeper DLP_{min} in the MAVAPs. The position of DLP_{min} lies between 171° and 177° of scattering angle for all MAVAPs at both wavelengths, without any clear trend linked to MAVAPs characteristics. In the case of the θ_{inv}, there is, on average, a slight shift toward larger scattering angles at 640 nm compared to 488 nm. No θ_{inv} values below 158° were experimentally observed. The presence of a strong NPB is typical of particles with irregularities at wavelength scale, which can generate negative polarization through single-particle effects and local multiple-scattering mechanisms (Shkuratov et al. 2004; Muinonen et al. 2011; Muñoz et al. 2021; Grynko et al. 2022). Therefore, the well-defined NPB observed for the MAVAPs is consistent with the sub-micrometer structures revealed by the SEM images (Figure 6).

4.3. Other scattering matrix elements

The third panels in Figures 7, 8, and 9 show $F_{22}(\theta)/F_{11}(\theta)$, which presents a consistent wavelength-dependent behavior for all MAVAPs. On average, the values at 488 nm are higher than those at 640 nm. At a given wavelength, there is also a clear color dependence. Dark MAVAPs display higher values of $F_{22}(\theta)/F_{11}(\theta)$ than light MAVAPs. Additionally, the curve shape shows a noticeable trend, more pronounced at 488 nm than at 640 nm. Beyond the minimum of $F_{22}(\theta)/F_{11}(\theta)$, light MAVAPs exhibit an increasing trend with convex curvature. In contrast, for dark MAVAPs the curvature changes from convex to concave as the scattering angle approaches the backscattering region.

The following panels present $F_{33}(\theta)/F_{11}(\theta)$, in which a clear wavelength dependence is observed. At 488 nm, the curves generally reach larger absolute values than at 640 nm. This difference becomes noticeable when the curves enter the negative region. For light MAVAPs, this wavelength trend is apparent over the entire angular range. In contrast, for dark MAVAPs the positive portions of the curves are more similar at both wavelengths, with differences becoming more noticeable mainly in the negative region. MAVAP-9 constitutes a partial exception to this behavior, as it exhibits significant wavelength differences even in the positive region, despite being classified as a dark MAVAP. Moreover, at a given wavelength, dark MAVAPs tend to exhibit deeper branch in the backscattering region than light MAVAPs.

The subsequent panels display $F_{34}(\theta)/F_{11}(\theta)$. For dark MAVAPs, the curves present a defined bell-shape profile, whereas for light MAVAPs this feature is weaker. The absence of a clear bell-shape is noticeable at 640 nm for MAVAP-2, MAVAP-3 and MAVAP-8. In several cases, the curves show both positive and negative regions, resembling the general behavior observed for $-F_{12}(\theta)/F_{11}(\theta)$. MAVAP-6 is especially remarkable, since its curves at both wavelengths are nearly identical over a broad angular range, but they clearly diverge once the negative region is reached.

The bottom panels show $F_{44}(\theta)/F_{11}(\theta)$, which exhibits a behavior similar to that of $F_{33}(\theta)/F_{11}(\theta)$. At scattering angles below 30° (the region of the $F_{11}(\theta)$ minimum) the values at 640 nm are slightly higher than those at 488 nm for dark MAVAPs. A similar tendency is also observed for MAVAP-5 and MAVAP-8 at smaller scattering angles. In the angular range in which the curves remain positive at both wavelengths, dark MAVAPs display very similar behavior at 488 nm and 640 nm, whereas light MAVAPs show clearly lower values at 640 nm. In the negative region, the curves at the two wavelengths diverge in all cases, being the results at 640 nm less intense (i.e., closer to zero) than those at 488 nm. Moreover, dark MAVAPs reach deeper negative values than light MAVAPs at both wavelengths. A distinctive feature appears close to 180° scattering angle, where an increasing tail is observed. This tail is stronger for dark MAVAPs at 488 nm. Particular attention should be given to MAVAP-9, which shows an intermediate behavior between dark and light groups, despite being classified as dark MAVAP.

The natural origin of MAVAPs can explain this behavior. Natural samples can be presented in a range of compositions, even if they originate from the same source. Therefore, a classification into two compositional groups may be quite simple, but it works well as a first approximation.

5. Discussion

In this section, we compare our experimental results to those of previous studies on dust of similar composition. We try to bridge the gap in understanding how particle size affects scattering behavior in the geometric optics regime. Additionally, we fit the backscattering region of the DLP curves using a widely adopted empirical mathematical expression commonly used in asteroid studies.

5.1. Size effect on geometric optics regime

To compare our measurements with those obtained for micron-sized dust clouds, we computed the arithmetic average of the normalized F_{ij} over all MAVAPs at each wavelength. This average matrix is used as a proxy for a cloud of millimeter-sized particles in the geometric optics regime. For the micron-sized comparison sample, we selected the JSC Mars-1 dust analyzed by Martikainen et al. (2024) for two main reasons. First, its bulk composition is dominated by palagonite, being also the case for the MAVAPs. Second, that study reported the scattering matrices measured at the same wavelengths as in our experiments. In that work, three JSC Mars-1 samples with increasing effective radius were investigated, denoted JSC-S (0.4 µm), JSC-M (2.7 µm), and JSC-L (16.5 µm). In addition, we compare our results at 640 nm with those obtained at 632.8 nm by Laan et al. (2009), since their palagonite powder and our MAVAPs originate from the same bulk. The palagonite powder analyzed in that study has an effective radius (4.5 µm) similar to JSC-M, but with a significantly broader size distribution.

Figure 10 shows the averaged MAVAP scattering matrix, together with the scattering matrices reported by Martikainen et al. (2024), at 488 nm (Figure 10a) and 640 nm (Figure 10b). We also include the results of Laan et al. (2009) at 632.8 nm in Figure 10b. The averaged MAVAP is presented by a solid line, while the shaded envelope indicates the range between the minimum and maximum values of the normalized F_{ij} at each scattering angle. This interval better reflects the variability expected for the simulated cloud than the propagated experimental errors. For JSC-S, only the phase function and DLP are available at both wavelengths. For JSC-M, the full scattering matrix is provided at 640 nm, whereas 488 nm only the phase function, DLP, and $F_{22}(\theta)/F_{11}(\theta)$ are available. For JSC-L, full scattering matrices are reported at both wavelength. The palagonite powder studied by Laan et al. (2009) includes the full scattering matrix at 632.8 nm. All phase functions are normalized to unity at 30° scattering angle. At both wavelengths, a clear difference in curve shape between the two size regimes is evident. The averaged MAVAP phase function exhibits the U-shape typical of few millimeter-size pebbles at visible wavelengths (Bertini et al. 2017; Muñoz et al. 2020), whereas the JSC powder clouds exhibit the typical slide-shape associated with micron-size dust (Munoz et al. 2001; Volten et al. 2006; Dabrowska et al. 2013; Escobar-Cerezo et al. 2018). This size-dependent behavior has also been reported by Muñoz et al. (2021) and Frattin et al. (2022). Therefore, our MAVAPs are far from reproducing the phase-function behavior of micron-size dust clouds.

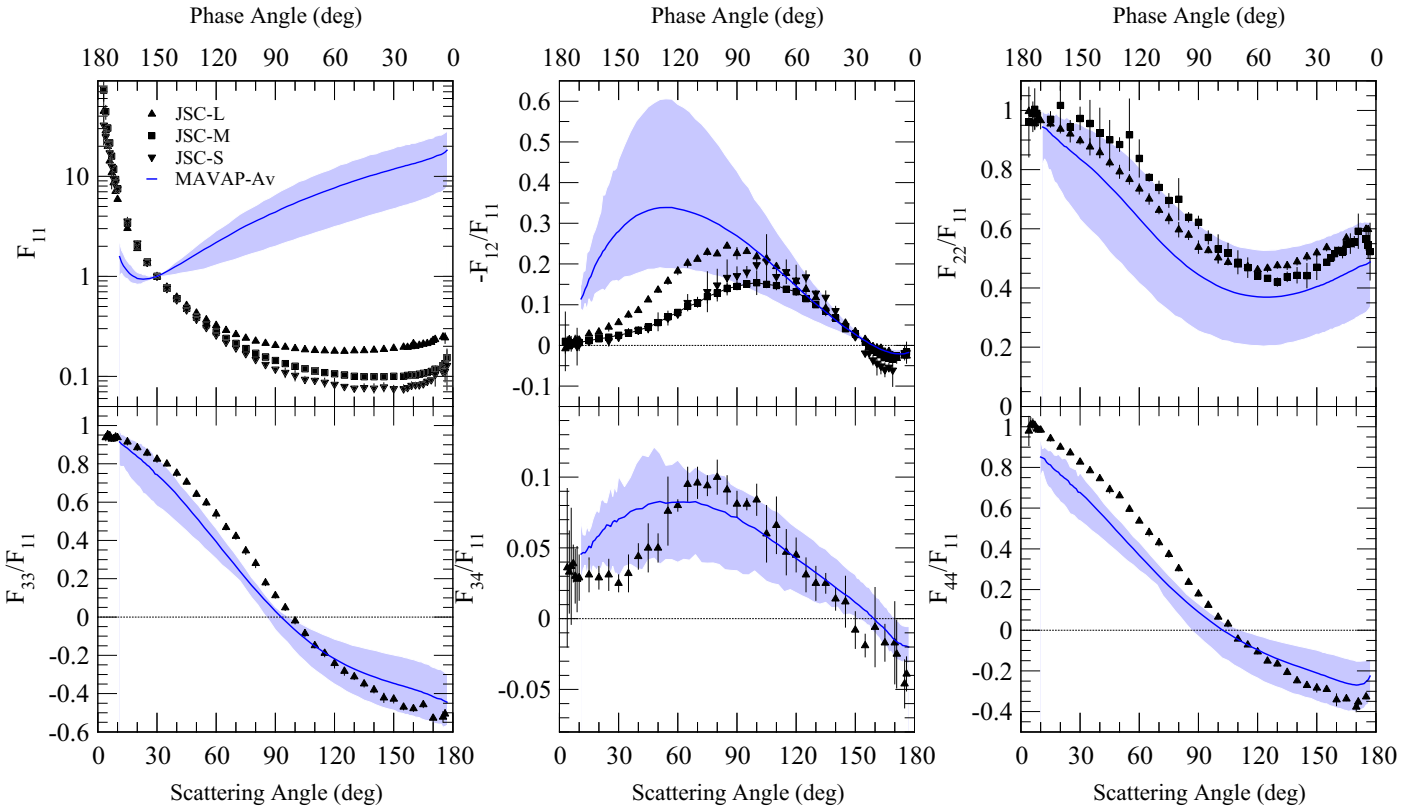
In the case of the DLP curves, θ_{max} clearly distinguishes micron-sized powder from millimeter-sized pebbles. At both wavelengths, θ_{max} shifts toward smaller scattering angles with increasing effective radius. The value of DLP_{max} primarily depends on the composition, and on the size regime in which particles are. Although palagonite is the main component in the JSC samples, variations in minor constituents and their relative abundances may affect the DLP amplitude. Particular attention should be given to the NPB, shown in Figure 11, where differences in DLP_{min} and θ_{inv} between JSC samples, the palagonite powder, and the averaged MAVAP become evident. At 640 nm, JSC-S and JSC-M differ significantly from the averaged MAVAP, whereas JSC-L displays remarkable agreement. Most JSC-L values are within the colored envelope and closely follow the averaged MAVAP curve over the angular range considered. Even θ_{inv} is very similar between JSC-L and the averaged MAVAP. The palagonite powder exhibits a comparable behavior to JSC-L, with small differences. Below θ_{inv} the palagonite powder shows slightly higher values (still within the shaded region), and beyond θ_{inv} the DLP values become a bit more negative than for the averaged MAVAP. At 488 nm, JSC-S and JSC-M tend to approach the averaged MAVAP behavior, although noticeable differences remain. The similarities between JSC-L and the averaged MAVAP persist at this wavelength as well. These results raise the important question of what the limits are of the DLP backscattering region as a discriminator between millimeter-sized pebbles and micron-sized dust clouds. As mentioned, DLP_{max} and θ_{max} are highly dependent on particle size. However, the DLP curves of the averaged MAVAP and the JSC-L powder are very similar at backscattering, particularly with regard to the NPB. This similarity has important implications for the interpretation of astronomical observations, since the slope at θ_{inv}, h, is often used as a proxy for the DLP_{max}. However, our experimental data show that samples exhibiting nearly identical NPB display significantly different DLP_{max} and θ_{max}.

For $F_{22}(\theta)/F_{11}(\theta)$, $F_{33}(\theta)/F_{11}(\theta)$, and $F_{44}(\theta)/F_{11}(\theta)$ at 640 nm, JSC-L displays a closer resemblance to the averaged MAVAP than to JSC-M or the palagonite powder. At red wavelengths, the palagonite powder behaves similarly to JSC-M for most normalized F_{ij}, except for $F_{44}(\theta)/F_{11}(\theta)$, where its behavior is more comparable to JSC-L. The similarity between the averaged MAVAP and JSC-L is significant for $F_{22}(\theta)/F_{11}(\theta)$, since their curves are almost indistinguishable. In contrast, at 488 nm this similarity in $F_{22}(\theta)/F_{11}(\theta)$ largely disappears. In this case, JSC-L becomes more similar to JSC-M, while JSC-M itself approaches the averaged MAVAP behavior more closely than at 640 nm. This loss of similarity for JSC-L at 488 nm is also observed for $F_{33}(\theta)/F_{11}(\theta)$ and $F_{44}(\theta)/F_{11}(\theta)$ when compared with their behavior at 640 nm. Conversely, at 488 nm $F_{34}(\theta)/F_{11}(\theta)$ of the averaged MAVAP appears to share more similarities with JSC-L than at 640 nm.

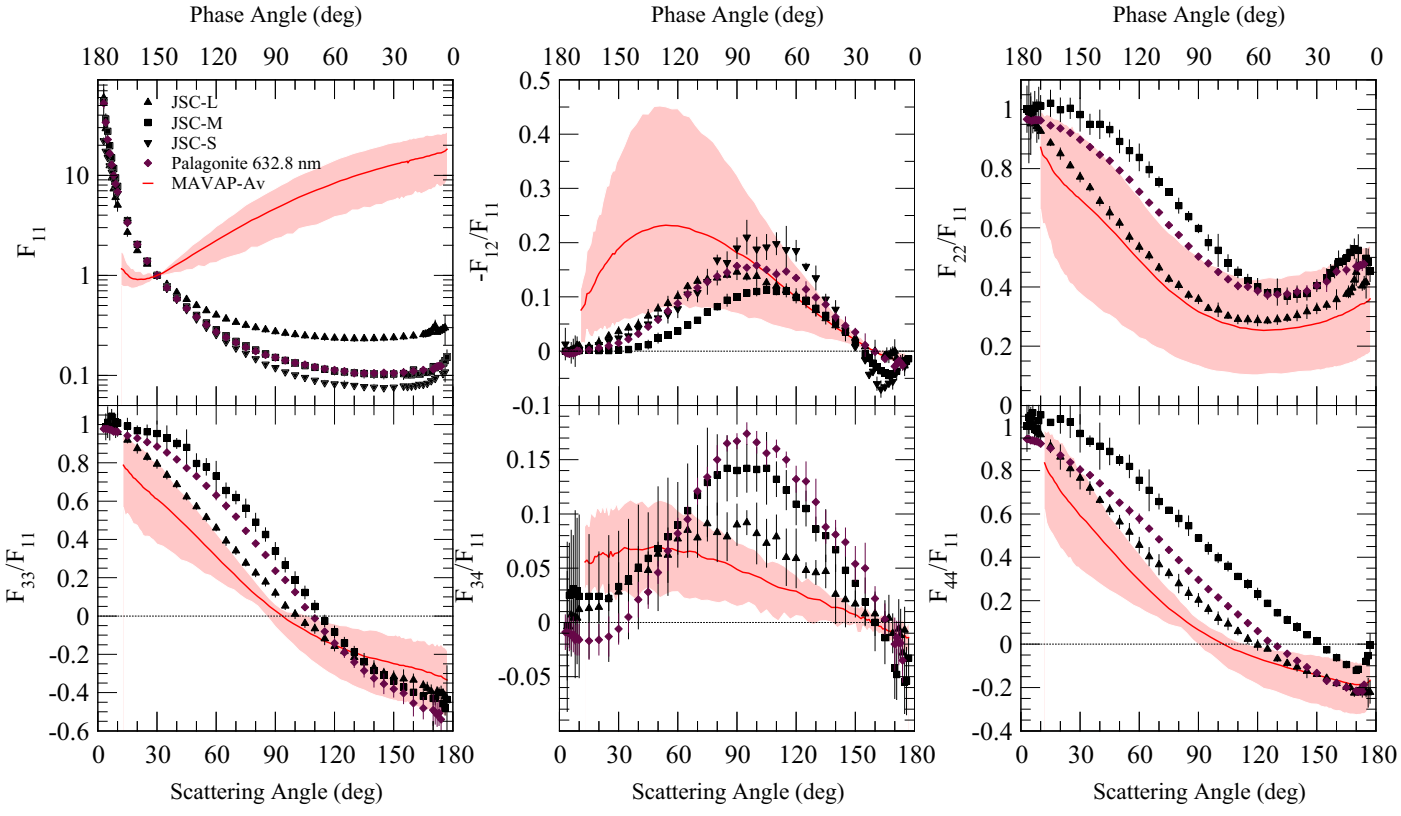
Overall, the comparison between the averaged MAVAP and JSC-L suggests that an increase in particle size from the transition region between the resonance and geometric optics domains produces significant effects in both phase function and DLP curves, whereas the other scattering elements exhibit only moderate variations. This suggests that the combination of the phase function and DLP curve constitutes a powerful diagnostic tool for constraining dust grain sizes in astronomical observations.

5.2. Photopolarimetry of astronomical bodies

The fact that MAVAPs and astronomical bodies, such as asteroids, appear very different at first glance does not make a



(a) 488 nm



(b) 640 nm

Fig. 10. Average scattering matrix of the nine MAVAPs. Solid lines represent the mean values and shaded areas indicate the variability range. The scattering matrix elements of the JSC micron-sized powder (Martikainen et al. 2024) and palagonite powder studied by Laan et al. (2009) are shown for comparison.

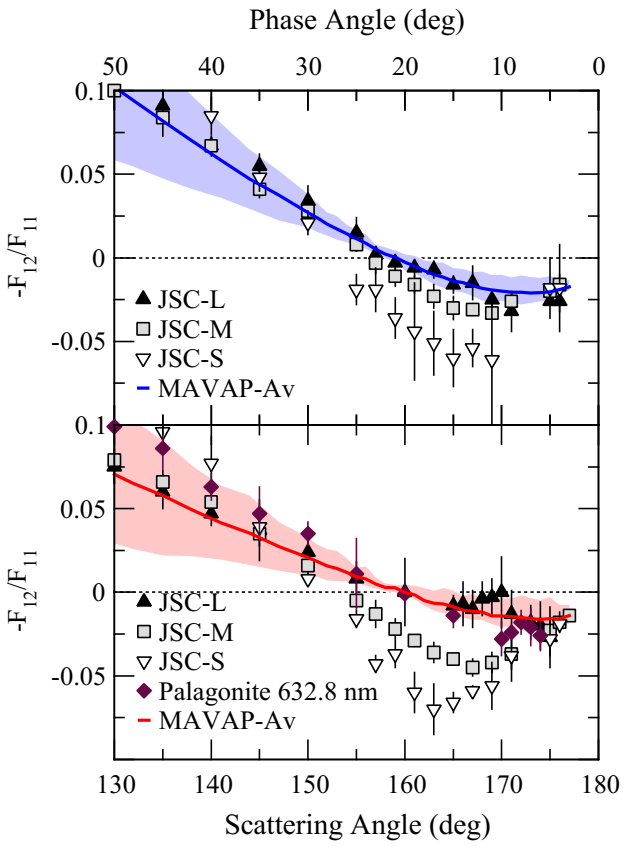


Fig. 11. NPBs for the MAVAP cloud, JSC powders, and palagonite powder (upper panel at 488 nm and bottom panel at 640 nm).

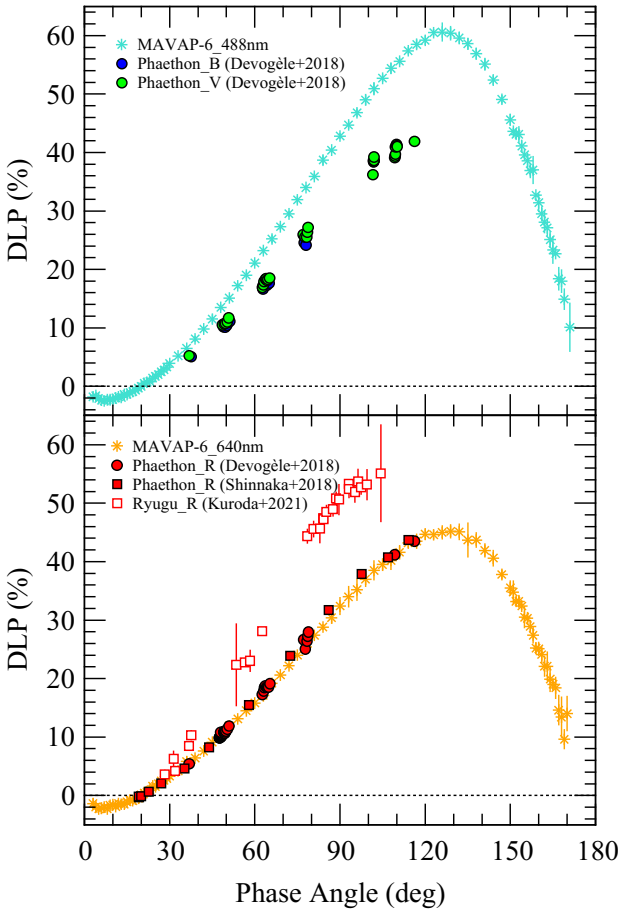


Fig. 12. Comparison of DLP curve observations of Phaethon and Ryugu with MAVAP-6 measurements. The upper panel shows MAVAP-6 results at 488 nm (turquoise stars) together with observations of Phaethon in the V filter (filled green circles) and B filter (filled blue circles) from Devogèle et al. (2018a). The lower panel shows MAVAP-6 results at 640 nm (orange stars), together with observations of Phaethon in the R filter from Devogèle et al. (2018a) (filled red circles) and Shinnaka et al. (2018) (filled red squares), as well as Ryugu observations in the R filter (white squares) from Kuroda et al. (2021).

comparison between them obvious. MAVAPs are millimeter-sized pebbles of volcanic ash, while asteroids range in size from tens of meters to kilometers. Nevertheless, the phase functions and DLP curves of the MAVAPs show an intriguing resemblance with those of the asteroids.

The phase function of the MAVAPs exhibit a well-defined U-shape (first row of Figures 7, 8, and 9), resembling that observed for some asteroids (Li et al. 2015; Shevchenko et al. 2019; Hergenrother et al. 2020). The MAVAPs display a phase-function minimum at large phase angles, while cometary dust observations made by Bertini et al. (2017), found this minimum at shorter phase angles. At such large phase angles, this minimum is inaccessible in asteroid observations. Additionally, the DLP curves of the MAVAPs (second row of Figures 7, 8, and 9) resemble those of asteroids (Jin et al. 2024), which exhibit maxima shifted toward large phase angles and in some case a high $DLP_{\max}$ as is the case for Phaethon (Shinnaka et al. 2018; Devogèle et al. 2018a) or Ryugu (Kuroda et al. 2021). Figure 12 shows the comparison between these two asteroids and MAVAP-6, which exhibits the highest $DLP_{\max}$ values at both studied wavelengths.

To explore the potential similarities between MAVAPs and asteroid observations, we analyzed and compared their polarimetric characteristics following the same approach commonly applied to asteroids. As an initial characterization, we derived the polarimetric color as a function of phase angle, $PC(\alpha)$ (Bagnulo et al. 2021; Gray et al. 2024a), for the MAVAPs using the following expression:

$$PC(\alpha) = \frac{|DLP^{\lambda_1}(\alpha)| - |DLP^{\lambda_2}(\alpha)|}{\lambda_1 - \lambda_2} 10^4, \quad (1)$$

where λ_1 and λ_2 correspond to the wavelengths 640 nm and 488 nm, respectively. The factor of 10^4 converts $PC(\alpha)$ into units of %/100 nm. The interpretation of $PC(\alpha)$ is straightforward. If $PC(\alpha) > 0$, the sample is considered polarimetrically red, whereas if $PC(\alpha) < 0$, it is polarimetrically blue. A value of $PC(\alpha) = 0$ indicates a neutral polarimetric color.

Figure 13 shows $PC(\alpha)$ (and $PC(\theta)$) for all MAVAPs, through the use of Eq. (1). Black and orange markers correspond to dark and light MAVAPs, respectively. Within the NPB, all MAVAPs exhibit a slightly blue or nearly neutral polarimetric color within error bars. This trend persists up to phase angles of about 30°. Beyond this angle, all MAVAPs exhibit a well-defined blue polarimetric color that becomes stronger with increasing phase angle (i.e., polarimetric phase blueing). Up to 90°, the MAVAPs exhibit a similar polarimetric phase blueing, with the exception of MAVAP-8, which shows a weaker effect. For phase angles larger than 90°, the dispersion among the MAVAPs increases. Around phase angles from 90° to 130°, the polarimetric phase blueing spans approximately from −7%/100 nm to −11%/100 nm. Despite this spread, no systematic trend can be identified which correlates the strength of the polarimetric phase blueing with specific MAVAPs properties. Moreover, the error bars largely overlaps in many cases, making the curves difficult

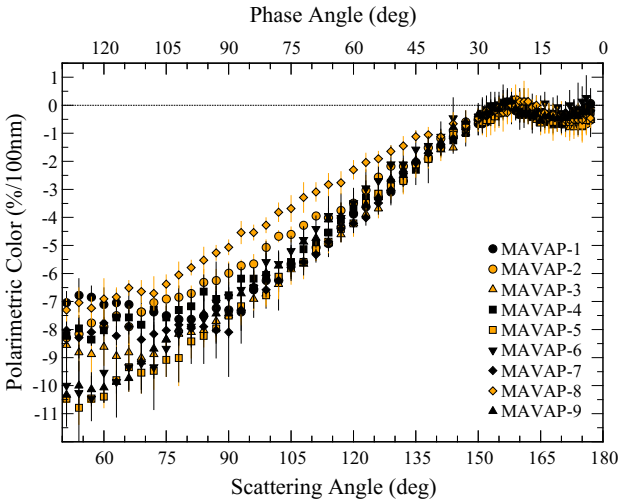


Fig. 13. Polarimetric color of MAVAPs. Marker colors indicate the sample visual appearance (black for dark ones, orange for light ones).

to distinguish from one another. A similar polarimetric blueing effect has been reported for some astronomical objects, as S-type and M-type asteroids, although with a weaker dependence on phase angle (Belskaya et al. 2009).

In addition to analyzing the polarimetric color, the polarimetric properties of the DLP can be investigated by fitting the measurements with a theoretical function. In order to characterize the features of the NPB, we adopt the linear-exponential expression as a function of phase angle, introduced by Kaasalainen et al. (2003) and Muinonen et al. (2009b):

$$DLP(\alpha) = A(e^{-B/\alpha} - 1) + C\alpha, \tag{2}$$

where A, B, and C are three free parameters. This empirical expression is widely used to analyze the DLP backscattering region of asteroid and comets (Cellino et al. 2015; Devogèle et al. 2018b; Gray et al. 2024b, 2025), providing key features for their classification (Belskaya et al. 2017). The model performs well up to phase angles of approximately 30° (Muinonen et al. 2009b). From the numerical fit, we can determine the inversion angle ($\alpha_{\rm inv}$), the phase angle at the minimum ($\alpha_{\rm min}$) and the corresponding DLP minimum ($DLP_{\rm min}$). The slope at $\alpha_{\rm inv}$, h, is then obtained by evaluating the derivate of Eq. (2) with respect to phase angle at $\alpha_{\rm inv}$:

$$h = \left.\frac{d\,\mathrm{DLP}(\alpha)}{d\alpha}\right|_{\alpha=\alpha_{\rm inv}} = A\,e^{-B/\alpha_{\rm inv}}\,\frac{B}{\alpha_{\rm inv}^2} + C. \tag{3}$$

Figure 14 shows the best-fit curves for each MAVAP obtained using Eq. (2). We limit the fitting range to phase angles up to 30° (vertical dotted lines), where the data density is highest and because some MAVAPs exhibit deep NPBs with rapid increase in the PPBs. To assess the quality of the fits, we calculated the normalized root-mean-square error (NRMSE) for each adjustment, summarized in Table 4. At 488 nm, NRMSE values range from 1.57% to 4.09%, while at 640 nm they range from 2.13% to 7.03%. Since all values are below 10%, the fits can be considered reliable. In addition to using the NRMSE, we analyzed the residuals normalized by the experimental uncertainties in Figure B.1 in the Appendix B. Two criteria indicate a reliable fit when examining them. First, most normalized residuals should fall within ±2, indicating discrepancies smaller than two experimental standard deviations. Second, they should be randomly distributed around zero without any systematic sign bias. Our fits satisfy both conditions, indicating that they are reliable. Comparing the experimental polarimetric parameters with their fit values, we find good agreement for $\alpha_{\rm inv}$, with similar values and overlapping error bars in all cases. A similar consistency is observed for $DLP_{\rm min}$, for which most cases show comparable values and overlapping uncertainties. In contrast, $\alpha_{\rm min}$ shows a slightly lower level of agreement. At 640 nm, some MAVAPs present non-overlapping uncertainties, and at 488 nm the light MAVAPs exhibit the largest differences. Although $\alpha_{\rm min}$ is reproduced less accurately than $\alpha_{\rm inv}$ and $DLP_{\rm min}$ and is more sensitive to composition, the agreement remains good.

We tested the fit curves by extending the angular range up to 50°. In most cases, the predicted values (beyond 30°) underestimate the experimental measurements, a trend more pronounced at 488 nm. An exception is MAVAP-6 at 640 nm, for which the predicted values slightly overestimate the experimental data. Overall, the extrapolated values cannot be considered fully reliable. Although some are close to the measurements, there is a systematic bias of under or overestimation. The normalized residuals in the extrapolated region further highlight this, showing both increased divergence and a consistent sign bias.

Table 4 summarizes the free parameters of Eq. (2) corresponding to the best fits (A, B, and C), together with the retrieved NPB features ($DLP_{\rm min}$, $\alpha_{\rm min}$, $\alpha_{\rm inv}$, and h) at 488 nm and 640 nm. Figure 15 presents the retrieved NPB features at 488 nm versus those at 640 nm. In these plots (hereafter referred to as parameter maps) the same markers as in Figure 13 are used.

The upper left panel of Figure 15 shows the parameter map for $|P_{\rm min}|$. The distribution of $|P_{\rm min}|$ clearly separates the MAVAPs into two groups related to color to naked eye. Dark MAVAPs exhibit higher $|P_{\rm min}|$ at both wavelengths compared to light MAVAPs. A common trend is that $|P_{\rm min}|$ is higher at 488 nm than at 640 nm. These results indicate that more absorbing MAVAPs tend to produce deeper $DLP_{\rm min}$. The upper right panel shows the parameter map for α_{inv}. The separation according to color is still visible, although less pronounced. Dark MAVAPs cluster toward the upper right direction of the plot, close to the 1:1 line, indicating that $\alpha_{\rm inv}$ is nearly achromatic for this group. Interestingly, MAVAP-6 lies on the opposite side of the 1:1 line compared to the rest of the MAVAPs. In contrast, light MAVAPs display a clear chromatic behavior, with larger $\alpha_{\rm inv}$ at 488 nm than at 640 nm. Within this group, MAVAP-8 shows the smallest $\alpha_{\rm inv}$ at both wavelengths, making it appear as an outlier. It also exhibits the largest deviation from the line 1:1, corresponding to the strongest chromatic dependence of $\alpha_{\rm inv}$ among the MAVAPs.

The bottom left presents the parameter map for h, in which the two groups are again well separated. In both groups, h is steeper at 488 nm than at 640 nm, and dark MAVAPs exhibit steeper h than light MAVAPs. Notably, MAVAP-6 appears to show the weakest chromatic dependence among dark MAVAPs. The bottom right panel shows the parameter map for $\alpha_{\rm min}$. Dark MAVAPs generally display larger $\alpha_{\rm min}$ than light MAVAPs. Similar to the behavior found for α_{inv}, MAVAP-6 shows larger $\alpha_{\rm min}$ at 640 nm than at 488 nm, contrary to the trend observed for the other MAVAPs. The relatively large error bars in $\alpha_{\rm min}$ at 640 nm for light the MAVAPs may be related with their lower absorption. Low absorbing MAVAPs tend to exhibit shallower and less well-defined NPBs, making the determination of $\alpha_{\rm min}$ more uncertain. Overall, these parameters maps illustrate how the retrieved polarimetric parameters are influenced by the intrinsic properties of the MAVAPs.

Additionally, Figure 16 presents the $DLP_{\rm min}$ - $\alpha_{\rm inv}$ parameter map. Same markers as in Figures 13 and 15 are used, but the incident wavelength is indicated by the color edge of markers,

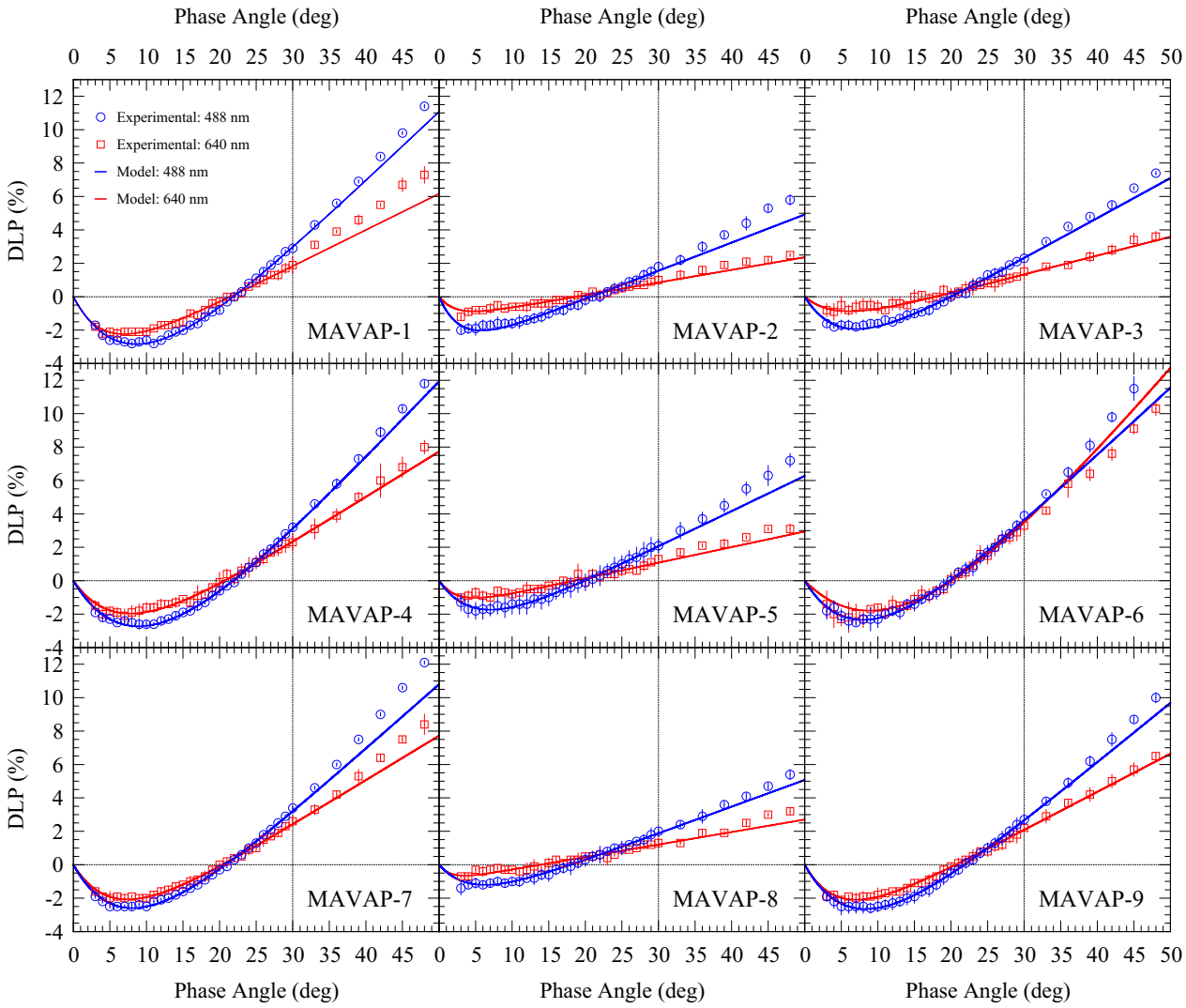


Fig. 14. Experimental NPB and best-fit curve obtained using Eq. (2), at 488 nm (blue) and 640 nm (red).

being blue for 488 nm and red for 640 nm. Each pair of points to the same MAVAP at different wavelengths is connected by a dotted line to highlight the wavelength dependence. This kind of parameter map is commonly used in the study of astronomical objects and in asteroid classification (Belskaya et al. 2010; Cellino et al. 2016; Bach et al. 2024).

With this parameter map it is possible to perform a qualitative classification of the MAVAPs as if they were asteroids, despite the possible differences in composition and structure between them. Although our measurements were not obtained exactly at the standard asteroid polarimetric wavelength, they fall within the typical BVR filter sequence, being 640 nm close to the R band and 488 nm lies between the B and V bands. We compare our $DLP_{\rm min}$ versus $\alpha_{\rm inv}$ results with those reported by Belskaya et al. (2010), Belskaya et al. (2017) and Belskaya et al. (2022). The dark MAVAPs exhibit $\alpha_{\rm inv}$ values between 19.5° and 22° at both wavelengths. Their $DLP_{\rm min}$ values are around −2% at 640 nm and become deeper at 488 nm. These characteristics are broadly consistent with those of C-type or Ch-type asteroids. The qualitative classification of the light MAVAPs is less straightforward. Except for MAVAP-8, the light MAVAPs at 488 nm display characteristics similar to those of the dark MAVAPs at 640 nm. However, at 640 nm they shift noticeably toward the upper left region of the $DLP_{\rm min}$–$\alpha_{\rm inv}$ map. This distribution places them in the intermediate zone of the parameter space, resembling the behavior of S-type asteroids. MAVAP-8 stands out, as it shows a relatively shallow $DLP_{\rm min}$ and a small $\alpha_{\rm inv}$, positioning it closer to the regions typically associated with S-type or even E-type asteroids.

The shapes of the phase function and DLP curves of our millimeter-sized pebbles are similar to those observed for asteroids, making our results directly relevant to the study of asteroid scattering behavior. Studies from the DART mission confirmed the presence of millimeter- to centimeter-sized particles in asteroid regoliths and impact ejecta (Moreno et al. 2023), underscoring the importance of precise experimental scattering data in this size range. That is also the case of the active asteroid Bennu, which loses mass by ejecting millimeter- to centimeter-sized particles (Hergenrother et al. 2020). Furthermore, the dense packing of particles in asteroid regoliths affects their scattering behavior. This invalidates the single scattering approximation and requires considering multiple scattering contributions (Pitman et al. 2005). In this context, Kolokolova et al. (2022) carried out pre-impact 3D radiative transfer simulations of the anticipated ejecta plume of the Didymos-Dimorphos system. Lolachi et al. (2023) demonstrated that using simplified isotropic phase functions rather than realistic experimental ones leads to large errors in the derived plume brightness and ejecta mass. Recent studies have demonstrated the value of using experimentally derived optical constants as inputs for modeling the scattering

Table 4. Fit values of DLP from 0° to 30° for each MAVAP at 488 nm and 640 nm using Eq. (2).

λ = 488 nm								
MAVAP	DLP_{min} (%)	α_{min} (deg)	α_{inv} (deg)	h (%/deg)	A (%)	B (deg^{-1})	C (%/deg)	NRMSE (%)
1	−2.84 ± 0.03	8.6 ± 0.1	21.85 ± 0.09	0.337 ± 0.005	9.7 ± 0.4	8.0 ± 0.4	0.41 ± 0.01	1.60
2	−2.0 ± 0.1	5.8 ± 0.5	20.7 ± 0.3	0.17 ± 0.01	3.5 ± 0.2	3.0 ± 0.5	0.17 ± 0.01	4.09
3	−1.93 ± 0.06	7.1 ± 0.2	19.9 ± 0.2	0.219 ± 0.005	4.9 ± 0.3	5.2 ± 0.5	0.24 ± 0.01	3.30
4	−2.73 ± 0.04	8.9 ± 0.1	21.9 ± 0.1	0.345 ± 0.006	11.2 ± 0.8	9.4 ± 0.6	0.46 ± 0.02	1.78
5	−1.7 ± 0.2	7.0 ± 0.9	19.9 ± 0.7	0.19 ± 0.02	4.3 ± 0.9	5 ± 2	0.21 ± 0.04	2.50
6	−2.3 ± 0.1	8.0 ± 0.4	19.8 ± 0.3	0.32 ± 0.01	9 ± 1	8 ± 1	0.40 ± 0.04	2.11
7	−2.60 ± 0.03	8.1 ± 0.1	20.80 ± 0.09	0.319 ± 0.004	8.5 ± 0.3	7.3 ± 0.4	0.39 ± 0.01	1.83
8	−1.21 ± 0.08	6.3 ± 0.6	18.0 ± 0.5	0.148 ± 0.006	2.9 ± 0.3	4 ± 1	0.16 ± 0.01	3.35
9	−2.7 ± 0.1	8.3 ± 0.4	21.8 ± 0.3	0.30 ± 0.02	8 ± 1	7 ± 1	0.36 ± 0.04	1.57
λ = 640 nm								
MAVAP	DLP_{min} (%)	α_{min} (deg)	α_{inv} (deg)	h (%/deg)	A (%)	B (deg^{-1})	C (%/deg)	NRMSE (%)
1	−2.24 ± 0.05	7.0 ± 0.3	21.4 ± 0.2	0.209 ± 0.009	4.7 ± 0.3	4.3 ± 0.4	0.22 ± 0.01	2.67
2	−0.87 ± 0.06	4.8 ± 0.8	18.7 ± 0.4	0.075 ± 0.005	1.4 ± 0.1	2.3 ± 0.7	0.076 ± 0.005	5.60
3	−0.9 ± 0.1	6 ± 1	17.9 ± 0.7	0.106 ± 0.006	2.0 ± 0.3	4 ± 2	0.11 ± 0.01	7.03
4	−1.96 ± 0.09	7.8 ± 0.4	20.7 ± 0.3	0.23 ± 0.01	5.9 ± 0.7	7 ± 1	0.27 ± 0.03	3.79
5	−1.03 ± 0.07	5.0 ± 0.5	18.4 ± 0.3	0.093 ± 0.005	1.72 ± 0.1	2.5 ± 0.5	0.093 ± 0.005	6.51
6	−1.79 ± 0.08	8.9 ± 0.4	20.1 ± 0.3	0.28 ± 0.01	14 ± 5	14 ± 4	0.5 ± 0.1	5.33
7	−2.08 ± 0.05	7.4 ± 0.2	20.4 ± 0.2	0.238 ± 0.007	5.6 ± 0.4	5.7 ± 0.5	0.27 ± 0.01	2.13
8	−0.65 ± 0.08	3.5 ± 0.8	13.9 ± 0.6	0.075 ± 0.004	1.0 ± 0.1	1.6 ± 0.7	0.075 ± 0.005	6.85
9	−2.09 ± 0.05	7.0 ± 0.3	20.6 ± 0.2	0.216 ± 0.008	4.8 ± 0.3	4.7 ± 0.5	0.23 ± 0.01	2.82

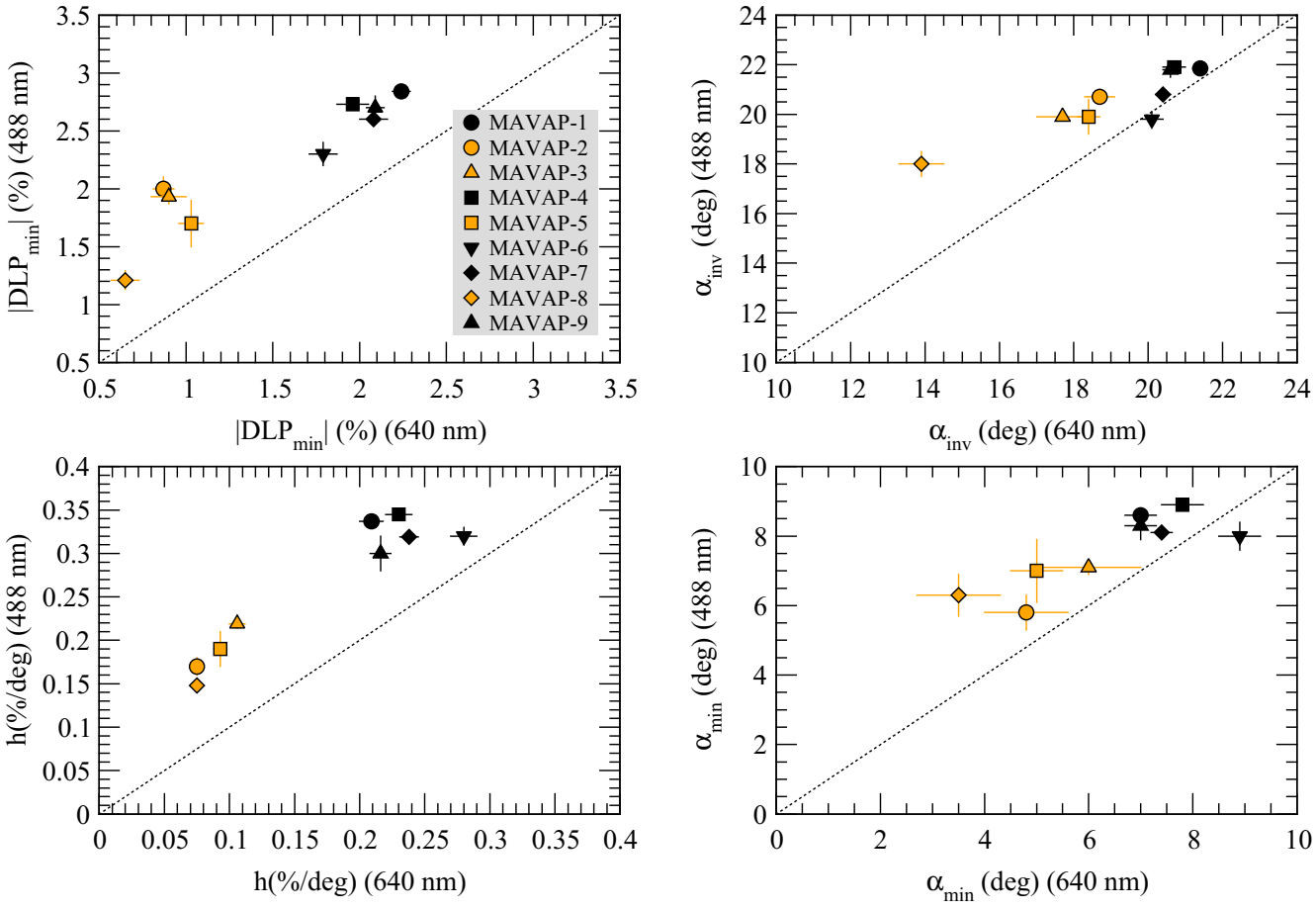


Fig. 15. Parameter maps of fit values for the MAVAPs, obtained using Eq. (2). Marker colors indicate the sample visual appearance (black for dark ones, orange for light ones).

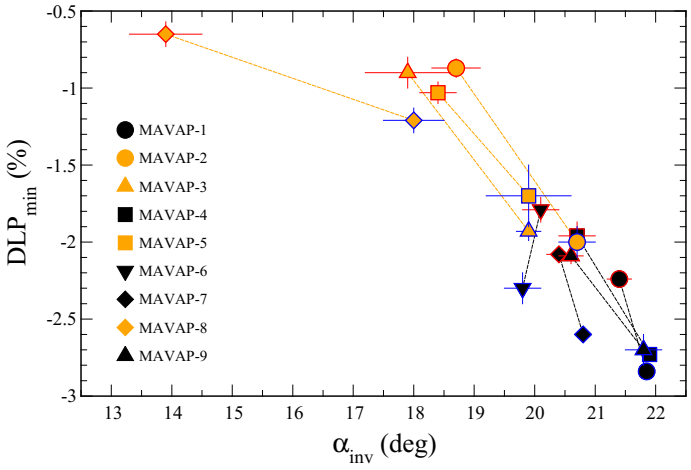


Fig. 16. DLP_{min} - α_{inv} parameter map for the MAVAPs, obtained by fitting Eq. (2). Edge colors indicate the wavelength used (blue for 488 nm, red for 640 nm), while marker colors indicate the sample visual appearance (black for dark ones, orange for light ones).

properties of asteroid regoliths and ejecta (Penttilä et al. 2024; Kolokolova et al. 2025). These studies highlight the importance of laboratory-derived optical inputs for radiative transfer modeling. Experimental phase functions and DLP curves, such as those presented in this work, offer complementary inputs that can improve the characterization of asteroid scattering behavior beyond simplified theoretical approximations.

6. Summary and conclusions

In this work, we present experimental scattering matrices at 488 nm and 640 nm for a set of individual millimeter-sized pebbles. The pebbles were levitated using an acoustic levitator, and the experimental setup was validated by measuring the scattering matrix elements of a well-characterized NBK-7 calibration sphere with a radius of 750 µm at both wavelengths. The studied set consists of nine volcanic ash pebbles (MAVAP), predominantly composed of palagonite. Their physical properties were characterized through optical and SEM imaging, as well as size estimations based on geometrical projections. According to their visual appearance, they were divided into two subsets (light and dark).

For the MAVAPs, the phase functions exhibit the characteristic U-shape reported in the literature for millimeter-sized particles in geometric optics regime. The DLP curves display a bell-shape profile, with θ_{max} at scattering angles smaller than 90°. A clear polarizing effect with absorption on the value of DLP_{max} is observed, with dark MAVAPs showing higher DLP_{max} compared to light MAVAPs. Well-defined NPBs are present, likely arising from the surface irregularities of the MAVAPs. Variations in the NPBs features with absorption are also detected, such as deeper DLP_{min} for dark MAVAPs compared to light MAVAPs. In general, all MAVAPs absorb more efficiently at 488 nm than at 640 nm. Depolarization effects in $F_{22}(\theta)/F_{11}(\theta)$, $F_{33}(\theta)/F_{11}(\theta)$, and $F_{44}(\theta)/F_{11}(\theta)$ are stronger at 640 nm than at 488 nm, and stronger for light MAVAPs than for dark MAVAPs. Overall, lower absorption appears to enhance the depolarization related to these normalized F_{ij}/F_{11} ratio of elements.

We compared the experimental results of the MAVAPs with those obtained for micron-sized dust samples of similar composition. The phase functions of the MAVAPs differ significantly from those of micron-sized dust, showing distinct curve shapes characteristic of their respective size regimes. The micron-sized powders tend to display a strong forward peak and nearly a flat behavior at side and back scattering regions. In contrast, the MAVAPs show a well-defined U-shaped phase function with minimum values in the phase angle region between 16° and 33°. The DLP curves also differ in the θ_{max}, which occurs at scattering angles near to or larger than 90° for micron-sized dust, and approximately between 48° and 66° for the MAVAPs. Interestingly, for dust composed of larger grains, the DLP curves tend to resemble those of the MAVAPs at scattering angles beyond approximately 130°. This similarity is more pronounced at the more strongly absorbed wavelength, making it difficult to clearly distinguish the NPBs of MAVAPs from those of micrometer-sized dust with larger monomers. This suggests that parameters such as the slope at θ_{inv}, h, should be used with caution as a proxy of DLP_{max}. There are also differences between the two size regimes for the remaining normalized F_{ij}. However, as the monomer size in the micron-sized dust increases, their normalized F_{ij} approach those of the MAVAPs.

In addition, we analyzed the MAVAPs as if they were asteroids. First, we derived their polarimetric color, which reveals a clear polarimetric phase blueing for all MAVAPs from α_{inv} toward larger phase angles. Within the NPB, the polarimetric color is slightly blue and becomes nearly neutral close to α_{inv}. Such polarimetric phase blueing is commonly observed in asteroids, suggesting a similar trend between asteroid surfaces and the MAVAPs. We also fit the NPBs using the well-known linear-exponential function developed by Kaasalainen et al. (2003) and Muinonen et al. (2009b). The fit curves reliably reproduce the NPBs within the angular range used for the adjustments (from 0° and 30° of phase angle). However, extrapolations beyond this range generally fail to accurately predict the DLP behavior. The fits allowed us to retrieve key NPB parameters and to explore their dependence on the physical properties of the MAVAPs. Access to measurements at two sufficiently separated visible wavelengths allowed us to investigate the chromatic behavior of the retrieved parameters. The MAVAPs exhibit sizes much larger than the wavelength of the incident light. Furthermore, we can assume similar surface roughness since they belong to the same bulk sample. Therefore, we can assume that their chemical composition dominates their scattering behavior. Finally, we attempted an approximate taxonomic classification of the MAVAPs using the DLP_{min}-α_{inv} map. Despite originating from the same natural bulk material, the MAVAPs occupy different regions of this parameter space according to their color. Dark MAVAPs tend to exhibit similar parameter values to as dark asteroids like C-type or Ch-type ones. In contrast, light MAVAPs tend to exhibit similar parameter values to S-type or even E-type asteroids. Nevertheless, the MAVAPs are much smaller than a whole ordinary asteroid, but their sizes could be representative for the pebbles covering the asteroidal regolith or the grains ejected by active asteroids (Hergenrother et al. 2020; Raducan et al. 2024). Moreover, our measurements are carried out in a visible wavelength region that is comparable with several astronomical observations of rocky bodies. This could indicate that for extremely large size parameter bodies, the nano and micro surface roughness might be more important than the macroscopic features.

This work represents the first application of the CoDuLab apparatus combined with an acoustic levitator to investigate the photopolarimetric properties of individual millimeter-sized pebbles. The results presented here open new possibilities for exploring novel types of samples, helping to bridge the existing

gap in the photopolarimetric behavior between micron-sized dust and regolith-like materials. This experimental setup will be used in future studies to further investigate the effect of physical properties on scattering behavior. We will study the effects of surface roughness and porosity introduced by the size distribution of the monomers that compose the agglomerates. These investigations will improve our understanding of light scattering produced by cometary and asteroidal dust.

Data availability

The experimental data are freely available at the Granada-Amsterdam light scattering database: `scattering.iaa.es` under request of citation of this paper and Muñoz et al. (2025).

Acknowledgements. We are grateful to L. Kolokolova for fruitful suggestions on a previous version of this manuscript. The authors acknowledge support from grant PID2021-123370OB-I00 and the Severo Ochoa grant CEX2021-001131-S, funded by MCIN/AEI/10.13039/501100011033. They also acknowledge support from grant PID2024-156713OB-I00 funded by MICIU/AEI/10.13039/501100011033. FJGI acknowledges support from grant PRE2022-103967 funded by MCIN/AEI/10.13039/501100011033. The authors thank Rocío Márquez Crespo from the Scientific Instrumentation Center of the University of Granada for providing the SEM.

References

Alvarez-Candal, A. 2024, A&A, 685, A29
Bach, Y. P., Ishiguro, M., Takahashi, J., et al. 2024, A&A, 684, A80
Bagnulo, S., Cellino, A., Kolokolova, L., et al. 2021, Nat. Commun., 12, 1797
Bagnulo, S., Belskaya, I., Cellino, A., et al. 2024, A&ARv, 32, 7
Banin, A., Han, F., Kan, I., & Cicelsky, A. 1997, J. Geophys. Res.: Planets, 102, 13341
Belskaya, I. N., Levasseur-Regourd, A.-C., Cellino, A., et al. 2009, Icarus, 199, 97
Belskaya, I., Fornasier, S., Krugly, Y. N., et al. 2010, A&A, 515, A29
Belskaya, I., Cellino, A., Gil-Hutton, R., et al. 2015, Asteroids IV, 151
Belskaya, I., Fornasier, S., Tozzi, G., et al. 2017, Icarus, 284, 30
Belskaya, I., Berdyugin, A., Krugly, Y., et al. 2022, A&A, 663, A146
Bertini, I., La Forgia, F., Tubiana, C., et al. 2017, MNRAS, 469, S404
Boehnhardt, H., Tozzi, G., Bagnulo, S., et al. 2008, A&A, 489, 1337
Cellino, A., Bagnulo, S., Gil-Hutton, R., et al. 2015, MNRAS, 451, 3473
Cellino, A., Bagnulo, S., Gil-Hutton, R., et al. 2016, MNRAS, 455, 2091
Colin, A., Muñoz, O., García-Izquierdo, F., et al. 2025, Exp. Astron., 59, 27
Dabrowska, D., Muñoz, O., Moreno, F., et al. 2013, JQSRT, 124, 62
Dabrowska, D. D., Muñoz, O., Moreno, F., et al. 2015, Icarus, 250, 83
Delahodde, C., Meech, K., Hainaut, O., & Dotto, E. 2001, A&A, 376, 672
Della Corte, V., Rotundi, A., Zakharov, V., et al. 2019, A&A, 630, A25
Devogèle, M., Cellino, A., Borisov, G., et al. 2018a, MNRAS, 479, 3498
Devogèle, M., Tanga, P., Cellino, A., et al. 2018b, Icarus, 304, 31
Escobar-Cerezo, J., Muñoz, O., Moreno, F., et al. 2018, ApJS, 235, 19
Fornasier, S., Hasselmann, P., Deshapriya, J. P., et al. 2020, A&A, 644, A142
Frattin, E., Muñoz, O., Moreno, F., et al. 2019, MNRAS, 484, 2198
Frattin, E., Martikainen, J., Muñoz, O., et al. 2022, MNRAS, 517, 5463
Frattin, E., García-Izquierdo, F. J., Martikainen, J., et al. 2025, A&A, 697, A137
García-Izquierdo, F. J., Frattin, E., Martikainen, J., et al. 2026, ApJS, 282, 49
Goidet-Devel, B., Renard, J., & Levasseur-Regourd, A. 1995, Planet. Space Sci., 43, 779
Gómez-Martín, J. C., Guirado, D., Frattin, E., et al. 2021, JQSRT, 271, 107761
Gómez-Martín, J. C., Muñoz, O., Martikainen, J., et al. 2023, ApJS, 270, 2
Gray, Z., Bagnulo, S., Boehnhardt, H., et al. 2024a, MNRAS, 531, 1638
Gray, Z., Bagnulo, S., Granvik, M., et al. 2024b, PSJ, 5, 18
Gray, Z., Bagnulo, S., Borisov, G., et al. 2025, ApJ, 992, L29
Grynko, Y., Shkuratov, Y., & Förstner, J. 2016, Opt. Lett., 41, 3491
Grynko, Y., Shkuratov, Y., Alhaddad, S., & Förstner, J. 2022, Icarus, 384, 115099
Hergenrother, C. W., Maleszewski, C., Li, J.-Y., et al. 2020, J. Geophys. Res.: Planets, 125, e2020JE006381
Hovenier, J. W., Van der Mee, C. V., & Domke, H. 2014, Transfer of Polarized Light in Planetary Atmospheres: Basic Concepts and Practical Methods, 318 (Springer Science & Business Media)
Ishiguro, M., Kuroda, D., Watanabe, M., et al. 2017, AJ, 154, 180
Jin, S., Ishiguro, M., Geem, J., et al. 2024, A&A, 690, A193
Kaasalainen, S., Piironen, J., Kaasalainen, M., et al. 2003, Icarus, 161, 34
Kahnert, M., Nousiainen, T., & Markkanen, J. 2016, in Light Scattering Reviews, 11: Light Scattering and Radiative Transfer (Springer), 299
Kimura, H., Kolokolova, L., Li, A., & Lebreton, J. 2016, in Light Scattering Reviews, 11: Light Scattering and Radiative Transfer (Springer), 363
Kolokolova, L., Jockers, K., Gustafson, B. Å., & Lichtenberg, G. 2001, J. Geophys. Res.: Planets, 106, 10113
Kolokolova, L., Hough, J., & Levasseur-Regourd, A.-C. 2015, Polarimetry of Stars and Planetary Systems (Cambridge: Cambridge University Press)
Kolokolova, L., Li, J.-Y., van Selous, M., Farnham, T., & Nagdimunov, L. 2022, PSJ, 3, 262
Kolokolova, L., Kelley, M. S., Kimura, H., & Hoang, T. 2024, Comets III, 621
Kolokolova, L., Markkanen, J., Ludet, Q., et al. 2025, PSJ, 6, 137
Kuroda, D., Geem, J., Akitaya, H., et al. 2021, ApJ, 911, L24
Kwon, Y. G., Ishiguro, M., Kwon, J., et al. 2019, A&A, 629, A121
Laan, E., Volten, H., Stam, D., et al. 2009, Icarus, 199, 219
Levasseur-Regourd, A. C., Renard, J.-B., Hadamcik, E., et al. 2019, A&A, 630, A20
Li, J.-Y., Helfenstein, P., Buratti, B., Takir, D., & Clark, B. E. 2015, Asteroids IV, 86, 277
Lolachi, R., Glenar, D. A., Stubbs, T. J., & Kolokolova, L. 2023, PSJ, 4, 24
Martikainen, J., Muñoz, O., Martín, J. C. G., et al. 2024, ApJS, 273, 28
Marzo, A., Barnes, A., & Drinkwater, B. W. 2017, Rev. Sci. Instrum., 88
Mie, G. 1908, Ann. Phys., 330, 377
Mishchenko, M. I. 2015, Measurement and modeling of electromagnetic scattering by particles and particle groups, Tech. rep., Cambridge University Press
Moreno, F., Guirado, D., Muñoz, O., et al. 2018, AJ, 156, 237
Moreno, F., Bagatin, A. C., Tancredi, G., et al. 2023, PSJ, 4, 138
Muinonen, K., Nousiainen, T., Lindqvist, H., Muñoz, O., & Videen, G. 2009a, JQSRT, 110, 1628
Muinonen, K., Penttilä, A., Cellino, A., et al. 2009b, Meteorit. Planet. Sci., 44, 1937
Muinonen, K., Tyynelä, J., Zubko, E., et al. 2011, JQSRT, 112, 2193
Muinonen, K., Penttilä, A., & Videen, G. 2015, in Polarimetry of Stars and Planetary Systems, 114
Munoz, O., Volten, H., De Haan, J., Vassen, W., & Hovenier, J. 2001, J. Geophys. Res.: Atmos., 106, 22833
Muñoz, O., Moreno, F., Guirado, D., et al. 2010, JQSRT, 111, 187
Muñoz, O., Moreno, F., Guirado, D., et al. 2011, Icarus, 211, 894
Muñoz, O., Moreno, F., Vargas-Martín, F., et al. 2017, ApJ, 846, 85
Muñoz, O., Moreno, F., Gómez-Martín, J. C., et al. 2020, ApJS, 247, 19
Muñoz, O., Frattin, E., Jardiel, T., et al. 2021, ApJS, 256, 17
Muñoz, O., Frattin, E., Martikainen, J., et al. 2025, JQSRT, 331, 109252
Nousiainen, T. 2009, JQSRT, 110, 1261
Ott, T., Drolshagen, E., Koschny, D., et al. 2017, MNRAS, 469, S276
Penttilä, A., Muinonen, K., Granvik, M., et al. 2024, PSJ, 5, 27
Pitman, K. M., Wolff, M. J., & Clayton, G. C. 2005, J. Geophys. Res.: Planets, 110
Polyanskiy, M. N. 2024, Sci. Data, 11, 94
Raducan, S., Jutzi, M., Cheng, A., et al. 2024, Nat. Astron., 8, 445
Rotundi, A., Sierks, H., Della Corte, V., et al. 2015, Science, 347, aaa3905
Roush, T. L., & Bell III, J. F. 1995, J. Geophys. Res.: Planets, 100, 5309
Shevchenko, V. G., Belskaya, I. N., Mikhalchenko, O. I., et al. 2019, A&A, 626, A87
Shinnaka, Y., Kasuga, T., Furusho, R., et al. 2018, ApJ, 864, L33
Shkuratov, Y., Ovcharenko, A., Zubko, E., et al. 2004, JQSRT, 88, 267
van de Hulst, H. C. 1981, Light Scattering by Small Particles (Courier Corporation)
Vargas, G., Guirado, D., Carrasco-González, C., et al. 2026, ApJ, 1004, 225
Volten, H., Muñoz, O., Brucato, J., et al. 2006, JQSRT, 100, 429
Volten, H., Muñoz, O., Hovenier, J., et al. 2007, A&A, 470, 377

Appendix A: Other scattering matrix elements

Figure A.1 presents the measured experimental scattering matrix elements for MAVAP-6 at 488 nm, as an example of the aspect of the measured scattering matrices for MAVAPs. These scattering matrix elements are presented as functions of the scattering (phase) angle. Off diagonal elements fulfill the relations $F_{12}(\theta)/F_{11}(\theta) = F_{21}(\theta)/F_{11}(\theta)$, $F_{34}(\theta)/F_{11}(\theta) = -F_{43}(\theta)/F_{11}(\theta)$, or they are zero within the experimental uncertainties. The element $F_{11}(\theta)$ is normalized by $F_{11}(30°)$.

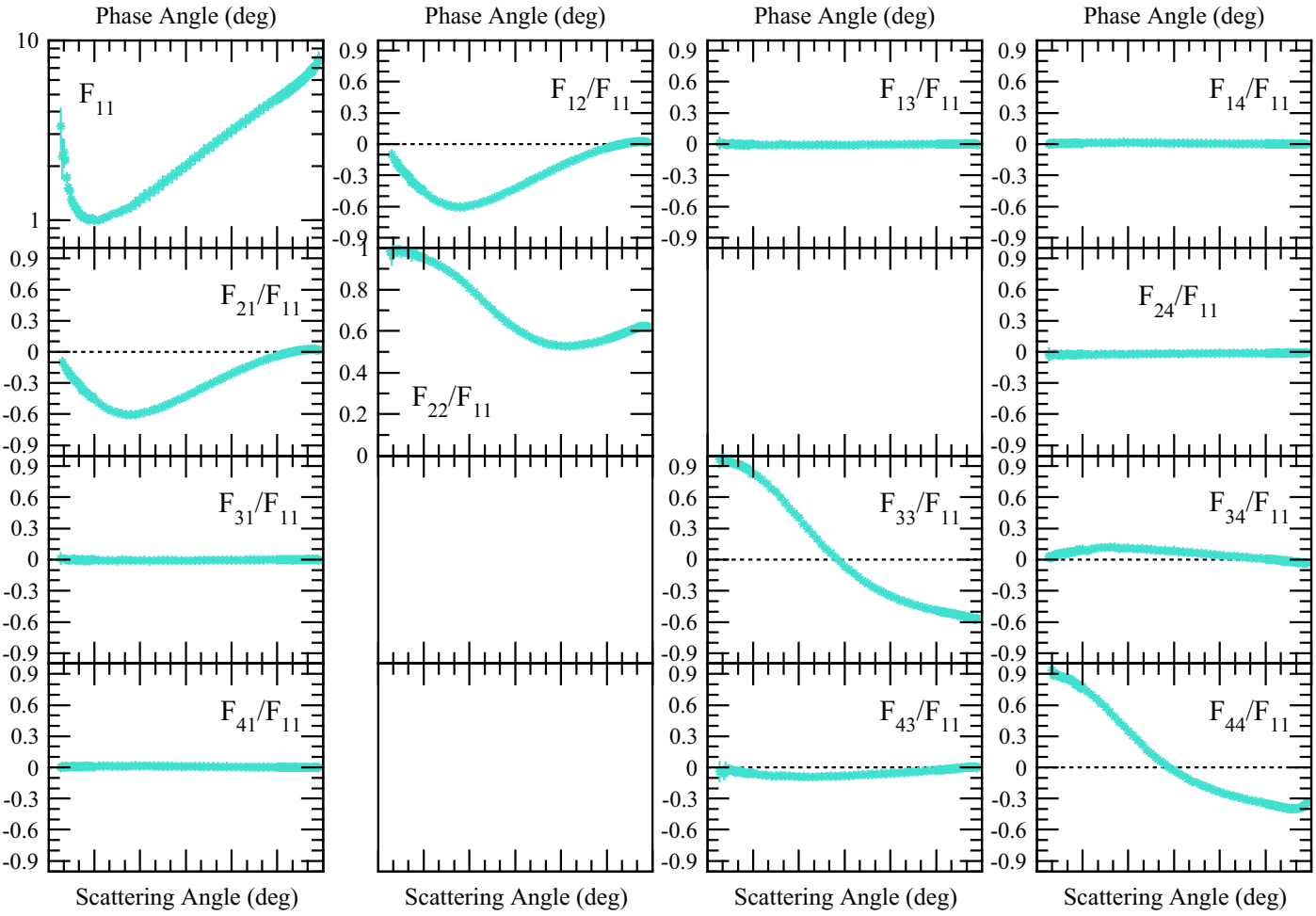


Fig. A.1: Experimental scattering matrix elements for MAVAP-6 as functions of the scattering (phase) angle at 488 nm.

Appendix B: Normalized residuals for the fits

Figure B.1 presents the residuals normalized by the experimental uncertainties. Most normalized residuals fall within ±2, indicating discrepancies smaller than two experimental standard deviations. Moreover, they are randomly distributed around zero without any systematic sign bias. These both conditions indicate that the fits are reliable.

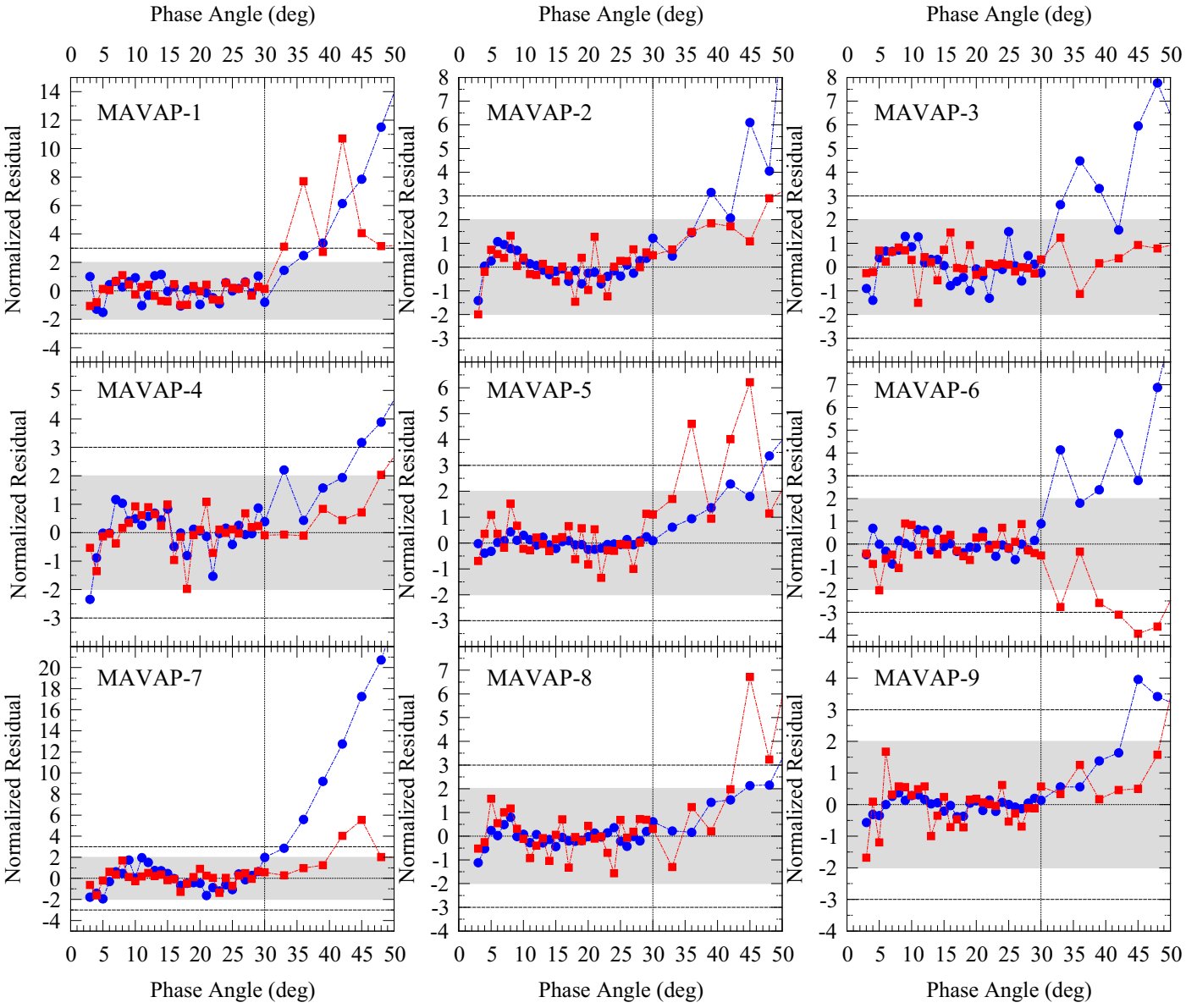


Fig. B.1: Normalized residuals for MAVAPs at each wavelength. The region of optimum values is presented in gray. The vertical dotted line is plotted at 30°. Values up to the dotted line correspond to the normalized residuals for the fits, while after the line they are for extrapolated values.